AGU PUBLICATIONS

Geochemistry, Geophysics, Geosystems

RESEARCH ARTICLE
10.1002/2015GC006236

Mass transfer in the lower crust: Evidence for incipient melt assisted flow along grain boundaries in the deep arc granulites of Fiordland, New Zealand

Catherine A. Stuart[1], Sandra Piazolo[1], and Nathan R. Daczko[1]

[1]Department of Earth and Planetary Sciences, ARC Centre of Excellence for Core to Crust Fluid Systems (CCFS) and GEMOC, Macquarie University, New, South Wales, Australia

Key Points:
- Replacement microstructures record a melt-rock hydration reaction in the lower crust
- Melt migrates through a grain boundary network facilitated by incipient melting of the host
- Incipient melt assisted flow may be an efficient mechanism of mass transfer in the crust

Correspondence to:
C. Stuart,
catherine.stuart@students.mq.edu.au

Citation:
Stuart, C. A., S. Piazolo, and N. R. Daczko (2016), Mass transfer in the lower crust: Evidence for incipient melt assisted flow along grain boundaries in the deep arc granulites of Fiordland, New Zealand, *Geochem. Geophys. Geosyst.*, *17*, 3733–3753, doi:10.1002/2015GC006236.

Received 21 DEC 2015
Accepted 25 AUG 2016
Accepted article online 29 AUG 2016
Published online 15 SEP 2016

Abstract Knowledge of mass transfer is critical in improving our understanding of crustal evolution, however mass transfer mechanisms are debated, especially in arc environments. The Pembroke Granulite is a gabbroic gneiss, passively exhumed from depths of >45 km from the arc root of Fiordland, New Zealand. Here, enstatite and diopside grains are replaced by coronas of pargasite and quartz, which may be asymmetric, recording hydration of the gabbroic gneiss. The coronas contain microstructures indicative of the former presence of melt, supported by pseudosection modeling consistent with the reaction having occurred near the solidus of the rock (630–710°C, 8.8–12.4 kbar). Homogeneous mineral chemistry in reaction products indicates an open system, despite limited metasomatism at the hand sample scale. We propose the partial replacement microstructures are a result of a reaction involving an externally derived hydrous, silicate melt and the relatively anhydrous, high-grade assemblage. Trace element mapping reveals a correlation between reaction microstructure development and bands of high-Sr plagioclase, recording pathways of the reactant melt along grain boundaries. Replacement microstructures record pathways of diffuse porous melt flow at a kilometer scale within the lower crust, which was assisted by small proportions of incipient melt providing a permeable network. This work recognizes melt flux through the lower crust in the absence of significant metasomatism, which may be more common than is currently recognized. As similar microstructures are found elsewhere within the exposed Fiordland lower crustal arc rocks, mass transfer of melt by diffuse porous flow may have fluxed an area >10,000 km^2.

1. Introduction

Geochemical signatures in upper crustal tonalite-trondhjemite-granites suggest that they are sourced from lower crustal or even mantle environments [e.g., *Bourdon et al*., 2002; *Gray and Kemp*, 2009; *Keay et al*., 1997; *Korhonen et al*., 2015; *Rapp et al*., 2003; *Vigneresse*, 2006]. However, details of the mechanisms responsible for mass transfer through the lower and middle crust are still under debate [*Brown*, 2004; *Petford*, 1996; *Weinberg*, 1996]. In the most general sense, mass is thought to migrate as a low viscosity phase, i.e., melt and/or supercritical fluid with or without solid components. Migration mechanisms are primarily controlled by pressure gradients, properties of the crust such as its porosity, elasticity and yield strength, and fluid properties such as buoyancy and viscosity [e.g., *Phipps Morgan and Holtzman*, 2005; *Sleep*, 1988; *Spence et al*., 1987]. Documentation of these mechanisms has principally relied on the crystallization of the migrating material, preserving evidence and structures of flow as well as indications of its composition. An understanding of mass transfer is of particular importance in modeling crustal evolution over time, especially in terms of chemistry and rheology. For example, differentiation of the crust and its compositionally layered structure is a direct result of mass transfer from the lower crust and upper mantle toward the surface [*Taylor and McLennan*, 1995]. Similarly, rheology of the lower crust is directly influenced by the presence and movement of low viscosity phases [*Holyoke and Rushmer*, 2002; *Rosenberg and Handy*, 2005], which in turn impacts patterns of brittle deformation in the upper crust [*Moresi and Mühlhaus*, 2006]. Therefore, a better knowledge of mass transfer in the crust is crucial in improving such models.

The two main mechanisms advocated for significant mass transfer through the crust occur during deformation, either within the brittle regime, through flow in dykes [e.g., *Sleep*, 1988; *Spence et al*., 1987; *Weinberg*, 1996] or the ductile regime, through flow in shear zones [e.g., *Beach and Fyfe*, 1972; *Carter and Dworkin*,

1990; *Cartwright and Barnicoat*, 2003; *Streit and Cox*, 1998]. Conceptually, there is also the possibility of a third mechanism, diffuse porous flow, which occurs without deformation and is commonly invoked in the mantle.

Diffuse porous melt flow (sensu stricto) is a process by which a melt migrates from its source rock and flows along grain boundaries through overlying units [*Scott and Stevenson*, 1986; *Turcotte and Ahern*, 1978]. As opposed to pervasive intrusion scenarios, where melt is distributed in meter-scale segregations forming dyke-like structures [e.g., *Vanderhaeghe*, 1999; *Weinberg and Searle*, 1998], diffuse porous flow occurs at the grain scale and melt is distributed in small pockets at grain boundaries and triple junctions. A key aspect of porous flow is that it occurs within a solid framework; in rocks, the solid framework breaks down at ~20–25% melt [*Vanderhaeghe*, 2009] and therefore porous flow can only occur at melt contents below this threshold. At low melt contents, melt geometry is controlled by dihedral angles between melt and two solid grains. When dihedral angles are small ($0° \leq \theta \leq 60°$), melt wets grain boundaries forming an interconnected network of channels [*Beere*, 1975; *von Bargen and Waff*, 1986], facilitating porous flow through the solid framework of the rock. Porous melt flow may be promoted if the migrating melt has a high water content, which has been shown to decrease dihedral angles allowing better connectivity [*Fujii et al*., 1986], and lower viscosity of the melt by several orders of magnitude, assisting flow [e.g., *Richet et al*., 1996; *Schulze et al*., 1996; *Shaw*, 1972].

Migration of melt via porous flow occurs in an open chemical system and therefore is accompanied by melt-rock reaction when the composition of the melt and rock are significantly different [*Spiegelman and Kenyon*, 1992]. Along the reaction front, local porosity variations result in fingering instabilities and focusing of flow into narrow zones. Termed porosity waves, these are zones of localized elevated porosity and focused porous flow in channels that are less than 1 km wide and up to tens of kilometers in height [*Bouilhol et al*., 2011; *Chadam et al*., 1986; *Connolly and Podladchikov*, 2007; *Scott et al*., 1986]. Relatively simple rock and melt compositions permit melt migration by diffuse porous flow to be well documented in the mantle where it results in significant chemical, mineralogical and rheological effects [e.g., *Dijkstra et al*., 2003; *Godard et al*., 1995; *Soustelle et al*., 2009]. Though a range of numerical studies exist proving viability in the crust [e.g., *Fountain et al*., 1989; *Jackson et al*., 2003, 2005; *Solano et al*., 2012], natural crustal examples of diffuse porous flow are limited. *Hasalová et al*. [2008a] describe a case of pervasive infiltration of an externally sourced melt that progressively reacts with the host orthogneiss, producing migmatitic textures requiring high fractions of melt. Open-system reactions between the solid host and migrating melt cause microstructural and chemical changes that allow identification of melt pathways and estimation of melt compositions [*Hasalová et al*., 2008b]. In general, porous flow can be buoyancy assisted, through the roof of an intrusion into overlying strata [*Solano et al*., 2012], however because the viscosity contrast between the host rock and migrating melt are not large, porous flow in the crust is thought to be largely deformation assisted, through a shear zone [*Hasalová et al*., 2008c]. Identification of porous flow in the crust is most likely hampered by the comparatively complex melt-rock reactions and overprinting of melt flow textures by metamorphic and/or tectonic events during exhumation.

The Pembroke Granulite, Fiordland, New Zealand, provides an exceptional opportunity to study the mechanisms of mass transfer in a high melt production zone as it is situated in a deep arc environment. The Pembroke Granulite was exhumed from depths of over 45 km [*Daczko et al*., 2001a, 2002a] with minimal tectonic and metamorphic overprint. Therefore, it provides a "window" into the deep crust where mass is transferred from the arc root to the upper crust. In the following, we document hydration reaction textures including microstructures indicative of the former presence of melt, along with distinct but subtle chemical changes from a micron to decimeter scale. Details of element distribution and reaction microstructures suggest a chemically open system bearing witness to significant mass transport by diffuse porous melt flow.

In the following, we define an *aqueous fluid* as a H_2O rich fluid with low dissolved solute content and a *hydrous silicate melt* as a silicate melt with a H_2O content at or below water saturation for given P-T-X conditions.

2. Regional Geology

The Pembroke Granulite, South Island, New Zealand, forms a ~15 km^2 low-strain zone within the Median Batholith, a composite regional batholith of Carboniferous to Early Cretaceous age [*Mortimer et al*., 1999].

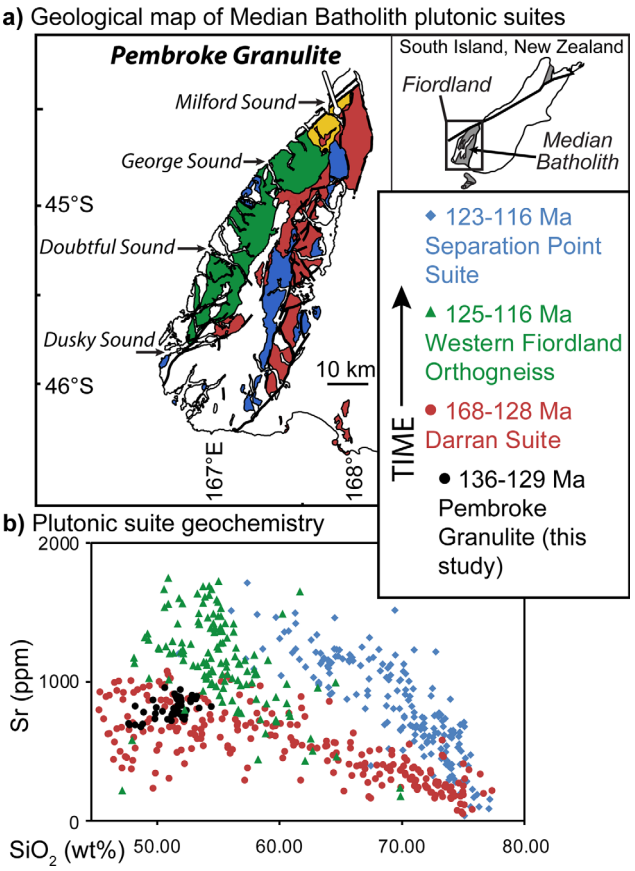

Figure 1. Regional setting of the Pembroke Granulite. (a) Geological map of Fiordland, New Zealand, showing selected plutonic suites of the Median Batholith. White pin points to the study area, the Pembroke Granulite, part of the Arthur River Complex (yellow). Inset shows outcrop of the Median Batholith and the region of Fiordland in the South Island of New Zealand. (b) Evolving SiO_2 versus Sr compositions of plutonic suites over time. The Pembroke Granulite has a low-Sr signature, consistent with the trend of the Darran Suite. Data: this study (Table 1); *Allibone et al*. [2009b]; *Allibone et al*. [2009c]; and *Hollis et al*. [2003].

The Median Batholith comprises suites of discrete plutons, representing a 250 m.y. record of arc magmatism. There are three main geochemical suites each characterized by a distinct age range and chemical signature (Figure 1). The long-term evolution of the arc system resulted in a switch from low to high Sr magmatism, observed at about 127 Ma (Figure 1b) [*Tulloch and Kimbrough*, 2003].

The Pembroke Granulite is situated within the metamorphosed and strongly deformed Arthur River Complex, Fiordland, New Zealand (Figure 1a) [overview in *Tulloch et al*. [2011]). It lies in the western part of the Median Batholith and has not formally been assigned to a geochemical suite. Suggested emplacement ages for the Pembroke Granulite range from 136–129 Ma [*Hollis et al*., 2003], to 163–150 Ma [*Stowell et al*., 2010], which together with other Arthur River Complex units predominately overlap ages advocated for the Darran Suite.

The Pembroke Granulite outcrops within the Pembroke Valley, where exposures span 1 km length, ~150 m width, and 220 m height. The Pembroke Granulite is principally a two-pyroxene-pargasite gabbroic gneiss. Relict igneous assemblages [e.g., *Chapman et al*., 2015; *Clarke et al*., 2013] are variably recrystallized by a pervasive S_1 gneissic foliation. The S_1 assemblage is defined by enstatite, diopside, pargasite, plagioclase, and ilmenite; published P-T estimates for orthopyroxene bearing assemblages vary from <6 to <11 kbar and 650–850°C [*Clarke et al*., 2000; *Daczko and Halpin*, 2009; *Stowell et al*., 2010]. Following the formation of the foliation, garnet reaction zones (GRZ) formed in narrow (cm – dm) zones in a mostly isochemical garnet granulite facies reequilibration of the host rock, thought to be triggered by the channelized intrusion of trondhjemitic melts [*Clarke et al*., 2005; *Daczko et al*., 2001b; *Schröter et al*., 2004; *Smith et al*., 2015] or sodic dehydration fluids [*Blattner*, 1976]. Formation of GRZ was likely to be long lived, with dates smearing from 126 to 122 Ma [*Stowell et al*., 2010] and estimated P-T conditions ranging between 11–14 kbar and 680–815°C [*Daczko et al*., 2001b; *Stowell et al*., 2010]. Subsequent deformation during exhumation was highly localized, preserving the lower crustal assemblage and microstructures throughout the majority of the Pembroke Granulite [*Blattner*, 1991; *Daczko et al*., 2001a; *Gardner et al*., 2016; *Smith et al*., 2015].

3. Methods

3.1. Major and Rare Earth Element Mineral Chemistry

Mineral chemistry was analyzed at the Geochemical Analysis Unit, CCFS/GEMOC, Macquarie University, Sydney, Australia, in order to characterize mineralogical changes and chemical environment during replacement. Major element chemistry was analyzed from polished thin sections using a CAMECA SX100 electron

microprobe (EMP). The EMP used five wavelength dispersive spectrometers to analyze spot sizes of 1–2 μm with an accelerating voltage of 15 kV and a beam current of 20 nA, counting for 3.5–5 min for each analysis.

Raw data from the EMP are recalculated to cations per formula unit for each mineral. For pyroxenes, the spreadsheet PX-NOM [*Sturm*, 2002] and classification diagrams and nomenclature following *Morimoto* [1988] are used. For amphiboles, the spreadsheet AMPH-CLASS [*Esawi*, 2004] and classification and nomenclature following *Leake et al*. [1997] are used.

Rare earth element (REE) chemistry was analyzed using laser ablation inductively coupled plasma mass spectrometry (LA-ICP-MS). A Photon Machines Excite excimer 193 nm laser ablation microprobe system was used to ablate 30–50 μm spots from minerals at a frequency of 5 Hz. Helium gas transported ablated material to the plasma at a flow rate of 0.8 L min^{-1}. Ablated material was analyzed in an Agilent 7700x inductively coupled plasma mass spectrometer (ICP-MS), using Ar as a carrier gas. External standards used were the NIST 610 glass and a basalt from the Columbia River (BCR-2). Internal standards used were aluminium (for orthopyroxene) and calcium (for all other minerals), both measured by EMP analyses. Raw signal data were reduced using the software GLITTER [*Griffin et al*., 2008].

3.2. Petrography and Backscatter Electron Images

Petrographic descriptions of polished thin sections used a petrographic microscope in combination with the Virtual Petrographic Microscope [*Tetley and Daczko*, 2014] and Image J v1.48a [*Rasband*, 1997−2015]. Backscatter electron (BSE) images were obtained of replacement microstructures to observe both small-scale microstructural details and chemical zonation. BSE images were collected from polished thin sections using a Carl Zeiss IVO scanning electron microscope (SEM) at the Geochemical Analysis Unit, CCFS/GEMOC, Macquarie University, Sydney, Australia. The SEM was run using an accelerating voltage of 15–20 kV, a beam current of 10 nA and working distances 10–12.5 mm.

3.3. Trace Element Mapping

High-resolution, high-sensitivity element mapping of the end member microstructures, termed Groups A and C below (PV1426 and PV1437, respectively), was performed on the X-Ray Fluorescence Microscopy beamline using the Maia-384 detector on the Kirkpatrick-Baez mirror microprobe at the Australian Synchrotron, Melbourne [*Paterson et al*., 2011; *Ryan et al*., 2010a]. A beam energy of 18.5 keV focussed to a spot size of 4 μm^2 was used. Samples analyzed were polished thin sections mounted on glass slides; no additional polishing or preparation was performed. Samples were scanned using a 4 μm step size in both the x and y directions, at a speed of 4.096 mm/s and a dwell time of 0.98 ms/pixel. Energy sensitivity of the Maia detector has a minimum of 3.3 keV, allowing detection of elements down to $Z = 20$ (Ca). A set of standard foils (Pt, Mn, Fe, YF_3) were periodically analyzed for calibration.

Real-time processing deconvolutes each individual X-ray event into element signals using the Dynamic Analysis (DA) method [*Ryan*, 2000; *Ryan et al*., 2010b], allowing rapid data collection along with high count rates and sensitivity. Data reduction was performed using GeoPIXE [*Ryan et al*., 1990], which uses the fundamental parameter model for the layered sample, the Maia detector efficiency model, and the DA matrix method to deconvolute spectra [*Ryan et al*., 1995, 2005]. Initially for both samples a plagioclase + amphibole matrix was used before refining the matrix correction to a pure plagioclase matrix using concentrations of values from analyzed features in the samples and mineral densities. Individual element maps for each sample were constructed.

3.4. Whole Rock Chemistry

Major and trace element whole rock compositions were obtained for representative samples characterized by each of the three replacement microstructure groups. Fresh samples of host rock of the Pembroke Granulite were powdered using a TEMA tungsten carbide mill, and then analyzed using X-Ray Fluorescence (XRF) spectroscopy. Five samples were analyzed at the Mark Wainwright Analytical Centre at the University of New South Wales, Sydney, Australia, using a PANalytical PW2400 Sequential WDXRF Spectrometer, calibrated using WROXI standards for major elements, and ProTrace standards for trace elements. Two samples were analyzed at the Geochemical Analysis Unit, CCFS/GEMOC, Macquarie University, Sydney, Australia. Major elements were analyzed using a PANalytical Axios 1KW WDXRF Spectrometer, calibrated with 60 international standards. Trace elements were obtained by solution Inductively Coupled Plasma Mass Spectrometry (ICP-MS), where digested samples were analyzed using an Agilent 7500 series instrument.

Table 1. Whole Rock Compositions of Representative Pembroke Granulite Gabbroic Gneiss Samples Obtained Using XRF and ICP-MS Analysis

Sample Name	PV1222	PV1320[a]	PV1307[a]	PV1230	PV1234	PV1216	PV1243
Dominant Microstructural Group	A	A	A	B	B	C	C
Majors (wt.% oxide)							
SiO_2	52.39	53.42	51.92	51.72	51.19	52.09	50.46
TiO_2	1.12	0.95	0.76	0.86	1.47	0.94	0.87
Al_2O_3	19.17	19.13	19.72	19.47	17.74	19.13	19.04
Fe_2O_3	9.12	8.41	8.28	8.70	10.28	8.52	8.72
Mn_3O_4	0.16	0.15	0.14	0.16	0.19	0.16	0.15
MgO	4.21	3.88	4.55	4.72	4.31	3.95	4.64
CaO	8.49	7.70	8.49	8.57	8.14	7.86	8.58
Na_2O	5.05	5.21	4.58	5.10	5.49	5.69	5.28
K_2O	0.49	0.64	0.38	0.39	0.52	0.50	0.40
P_2O_5	0.22	0.31	0.20	0.18	0.39	0.29	0.22
SO_3	<0.01[c]			0.01	<0.01	<0.01	<0.01
L.O.I.[b]	*0.60*	*0.01*	*0.00*	*0.93*	*0.62*	*0.73*	*0.97*
Total	101.00	99.80	99.02	100.80	100.35	99.85	99.33
Traces (ppm)							
Li		7.69	9.13				
Be		1.11	0.86				
Sc		24.35	23.70				
Ti		5882	4804				
V	266	186.1	211.6	236	273	210	246
Cr	20	11	15	22	23	21	25
Mn		1134	1091				
Co	69	56.56	58.04	89	56	62	77
Ni	10	16.1	20.7	13	12	13	16
Cu	79	107.9	37.6	163	66	48	57
Zn	84	85.3	75.0	85	103	88	85
Ga	20	20.50	20.69	19	19	20	20
As	3			4	3	4	4
Rb	4	2.96	2.09	4	3	3	3
Sr	796	812.7	943.6	788	720	742	788
Y	8	16.84	10.34	6	15	11	9
Zr	49	17.2	11.0	41	49	43	40
Nb	<1	2.08	0.86	<1	1	<1	<1
Mo	<2	0.42	0.18	2	<2	2	<2
Cd	<3	0.053	0.044	<3	<3	<3	<3
Sn	<4			<4	<4	<4	<4
Sb	<3			<3	<3	<3	<3
Cs		0.111	0.204				
Ba	244	379.9	256.7	201	300	301	213
Ta		0.679	0.538				
Pb	8			8	10	10	9
Th	<3	0.339	0.170	<3	<3	<3	<3
U	<3	0.091	0.047	<3	<3	<3	<3
REE (ppm)							
La		10.49	6.31				
Ce		23.11	13.88				
Pr		3.17	1.85				
Nd		14.21	8.35				
Sm		3.33	1.97				
Eu		1.209	0.948				
Gd		3.21	1.96				
Tb		0.479	0.290				
Dy		2.67	1.66				
Ho		0.552	0.346				
Er		1.523	0.951				
Yb		0.202	0.129				
Lu		0.603	0.361				

[a]Samples analyzed at Macquarie University, trace and REE by solution ICP-MS. Elements analyzed differed between laboratories.

[b]L.O.I. = Loss on ignition.

[c]A less than symbol (<) denotes concentrations below the stated value of the lower limit of detection.

3.5. Thermodynamic Modeling

Thermodynamic modeling in the model NCKFMASHTO (Na_2O-CaO-K_2O-Fe_2O_3-MgO-Al_2O_3-SiO_2-H_2O-TiO_2-Fe_2O_3) was undertaken to obtain constraints on P-T conditions at which replacement microstructures formed. Although the replacement microstructures are arguably disequilibrium textures, the lack of correlation between composition and degree of replacement warrants the approximation of P-T conditions through pseudosection analysis. The whole rock composition of sample PV1216 (Table 1), a sample characterized by Group C replacement microstructures, is used on the basis that nearly the entire volume of the sample approached equilibrium with the passing melt, as evidenced by little to no major element chemical zonation in individual constituent minerals. X-ray fluorescence data are recalculated into mole proportions as input for THERMOCALC.

Modeling was undertaken using the software THERMOCALC 3.33 [*Powell and Holland*, 1988] and the internally consistent data set of *Holland and Powell* [2011] (data set tcds55). Minerals modeled in the pseudosection include hornblende (hb; *Diener et al.* [2007]), diopside (di; *Green et al.* [2007]), biotite (bi; *White et al.* [2007]), garnet (g; *White et al.* [2007]), muscovite (mu; *Coggon and Holland* [2002]), paragonite (pa; *Coggon and Holland* [2002]), plagioclase (pl; *Holland and Powell* [1998]), epidote (ep; *Holland and Powell* [1998]), silicate

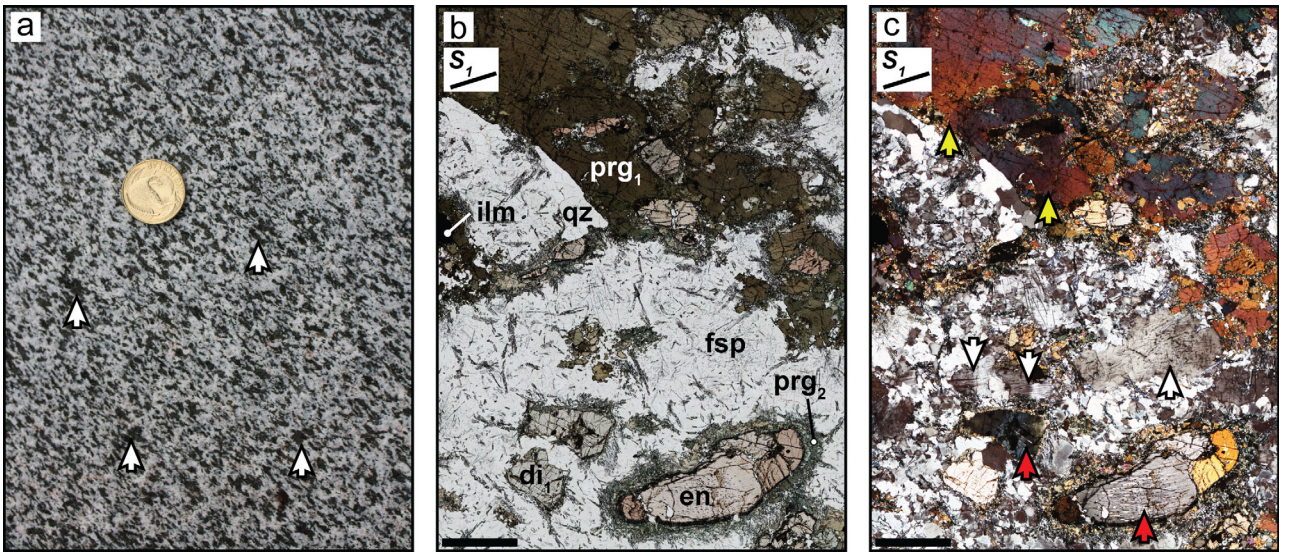

Figure 2. General characteristics of the Pembroke Granulite. (a) Characteristic outcrop of the gabbroic gneiss. White arrows indicate some of the coarse-grained pargasite (prg_1). (b) and (c) Photomicrograph of a typical gabbroic gneiss (PV1448) in Figure 2b plain-polarized light and Figure 2c crossed polarized light. S_1 orientation marked in top left. Scale bar is 1000 μm. (b) S_1 foliation in the gabbroic gneiss is defined by enstatite, diopside and pargasite (prg_1). Note asymmetry in the corona around grain labelled di_1. (c) Deformation features in S_1 mineral assemblage; white arrows highlight large plagioclase grains with undulose extinction surrounded by small, recrystallized grains. Yellow arrows and red arrows highlight igneous amphibole and pyroxene grains with undulose extinction.

melt (liq; *White et al*. [2007]), magnetite (mt; *White et al*. [2002]), ilmenite (ilm; *White et al*. [2000]), rutile (ru), titanite/sphene (sph), and quartz (q). The amphibole model used in this study [*Diener et al*., 2007] does not currently include potassium, of which up to 2 wt.% was measured in amphiboles from the sample. This forces low amounts of biotite to be stable in the assemblages (1–5 vol.%), and results in a slight underestimation of the mode of amphibole. The melt model used in this study [*White et al*., 2007] is for felsic rocks. In applications on intermediate to mafic compositions, *De Paoli et al*. [2012] showed that this model is valid for predicting the location of the solidus, but was invalid at >5% melt. We therefore consider the model adequate for this study, as we interpret the pseudosection only at low modes of melt.

The amount of H_2O used in the model is a critical factor in determining both mineral stability fields and the solidus position. A T-X_{H2O} diagram (Figure 7a) was constructed to constrain the H_2O content during replacement microstructure formation, using a loss on ignition lower than that measured in the natural sample as a minimum value of H_2O (0.40 wt.%), and a loss on ignition approximately seven times larger as a maximum (2.73 wt.%). The observed mineral assemblage was stable between 0.63 and 2.23 wt.% H_2O, encompassing fields both above and below the solidus. Mineral proportions and chemistry in the natural sample best match 0.85 wt.% H_2O, which has been used to construct the P-T pseudosection (Figure 7).

The amount of Fe_2O_3 is recast as "O" in the NCKFMASHTO model. Several methods were employed in order to estimate the amount of Fe_2O_3 in the bulk rock composition. Initially, the amount was estimated using a ratio of 0.08 $Fe^{3+}/\Sigma Fe$, as per *Daczko and Halpin* [2009]. However, the resulting P-T pseudosection lacked a field with the observed mineral assemblage, and had discrepancies between calculated and measured mineral compositions and garnet being stable at low pressures. Predicted garnet stability at low pressures was interpreted as an underestimation of the Fe_2O_3 content and so the linear relationship between Ba/La ratio and $Fe^{3+}/\Sigma Fe$ ratio [*Kelley and Cottrell*, 2009] was used to refine the estimate of the Fe_2O_3 content for the model. Ba/La ratios in gabbroic gneisses of the Pembroke Valley range between 30 and 100, corresponding to $Fe^{3+}/\Sigma Fe$ ratios between 0.20 and 0.32. The average Ba/La ratio for the natural samples (54.54) produced a $Fe^{3+}/\Sigma Fe$ ratio of 0.24, and a P-T pseudosection containing a field with the observed mineral assemblage.

4. Results

4.1. General Characteristics of the Pembroke Granulite

At the outcrop scale, the gabbroic gneiss appears relatively homogeneous with minor variations in grain size and strain; the latter is inferred from differences in foliation intensity. In addition, subtle color changes

can be observed when focusing on the mafic phases of the rock (Figure 2a). Thin section analyses confirm differences in the phase percentages of pyroxene and pargasite, where pargasite may occur as large grains (prg_1, Figure 2b) or as small grains associated with pyroxene reaction microstructures (prg_2, Figure 2b).

Partial reaction microstructures of enstatite and diopside grains to pargasite and quartz are observed in the gabbroic gneiss. Detailed examination of exposures as well as extensive sampling of the entire outcrop available in the Pembroke Valley show that these features are ubiquitous. The spatial distribution of the reaction microstructures is heterogeneous across a millimeter scale.

4.2. Detailed Microstructures and Mineral Chemistry

4.2.1. Gabbroic Gneiss Without Reaction Microstructures

Portions of the gabbroic gneiss lacking reaction microstructures contain semirectangular domains of plagioclase (pl_1, Ab [100*Na/{Ca + Na + K}] = 54–62; 40–50 vol.%; Figure 3a) and elongate clusters (50–60 vol.%) of deformed anhedral diopside (di_1, Mg# [100*Mg/{Mg + Fe^{2+}}] = 72–89, Figures 3b and 3c) and enstatite (en, Mg# = 57–64; Figure 3c) each up to 5 mm in length. Pyroxenes are coarse grained (1000–6000 μm) and

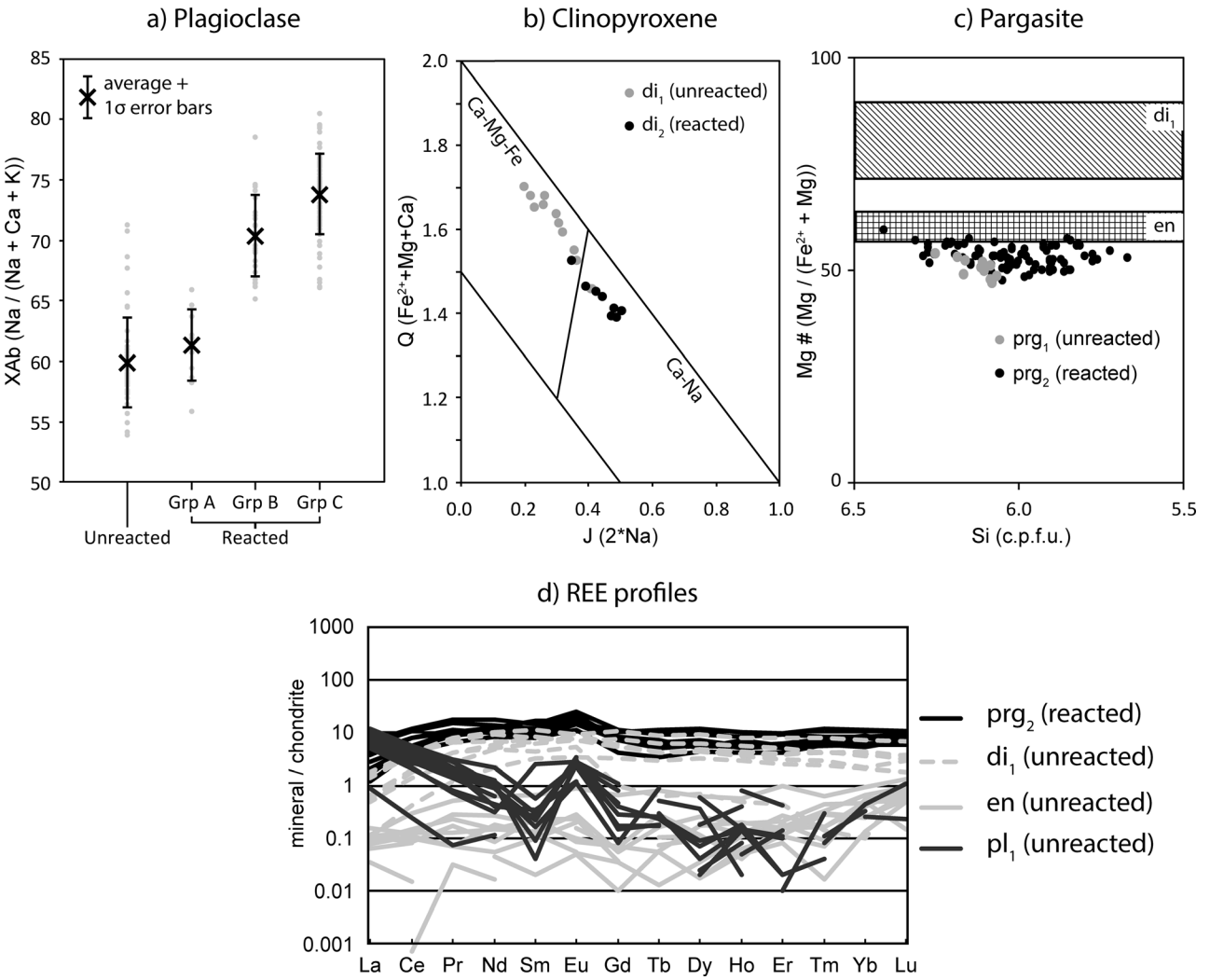

Figure 3. Major element chemistry of minerals in replacement microstructures compared to those from the unreacted igneous assemblage. (a) Albite compositions of plagioclase grains from the gabbroic gneiss without reaction microstructures (unreacted) and from the three reaction microstructural groups, A, B, and C. Gray dots indicate range in natural samples, black crosses indicate the average value with 1σ error bars. Note the increasing albite content with degree of replacement. (b) Q-J classification diagram for clinopyroxenes. Plotted are igneous, unreacted diopside (di_1), and sodic diopside from reaction microstructures (di_2). Note increased Na content in di_2. (c) Si (c.p.f.u.) versus Mg# of unreacted pargasite grains, and pargasite grains in reaction microstructures replacing both igneous enstatite (en) and diopside (di_1). Cross-hatched field indicates the range in Mg# for enstatite; striped field indicates the range in Mg# for diopside. Note the consistently low Mg# of prg_2, despite high values of parent pyroxenes. (d) REE profiles of reactant pyroxene and plagioclase and product pargasite in reaction textures. Note the enriched patterns of pargasite compared to the mostly depleted patterns of pyroxenes and plagioclase.

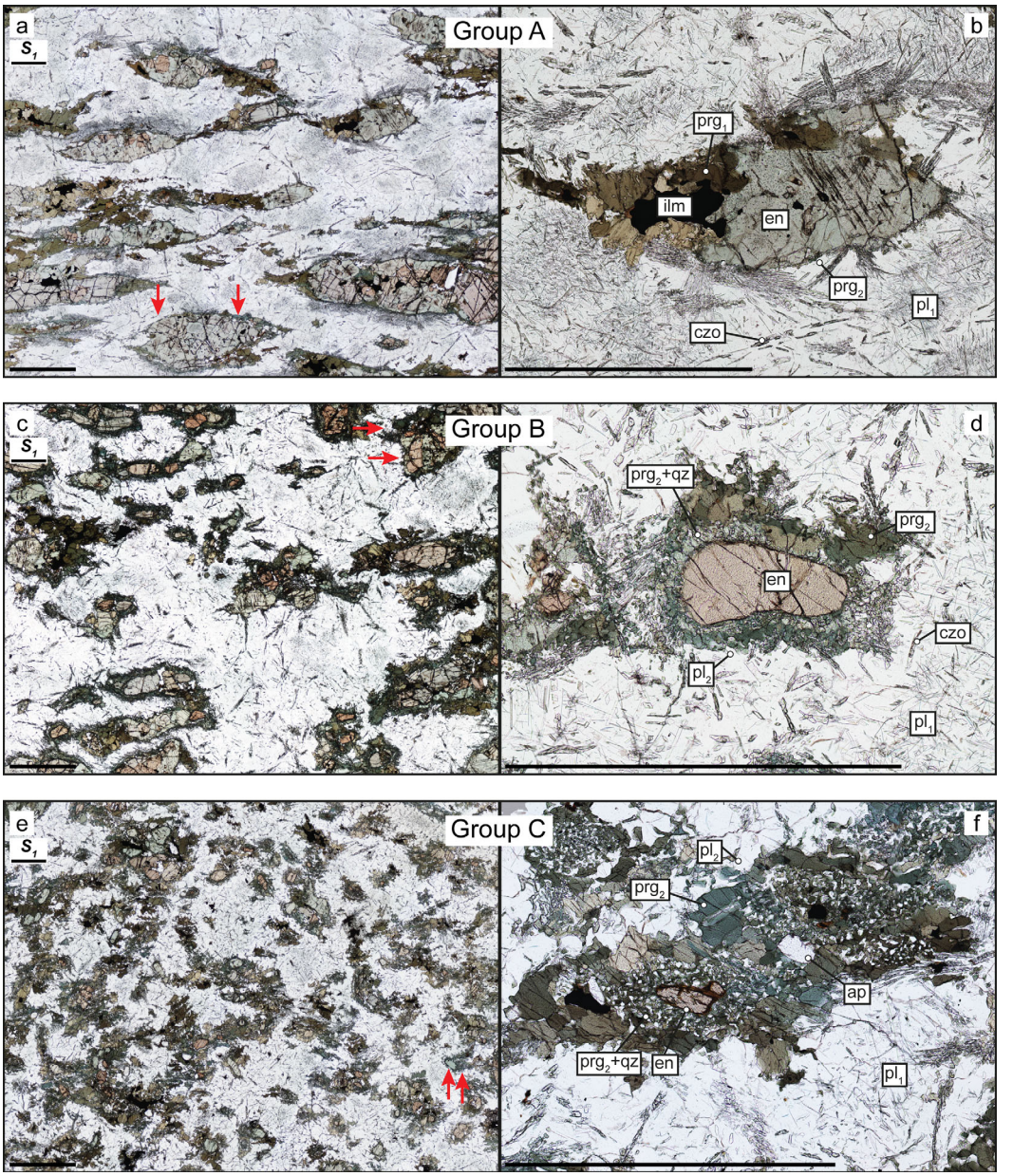

Figure 4. Photomicrographs of replacement microstructures, S_1 orientation marked on overview images. Scale bars 2000 μm. Red arrows highlight discontinuous and/or asymmetric replacement microstructures. (a) and (b) Sample characterized by Group A microstructures (PV1426). (a) Overview. (b) A typical Group A microstructure. (c) and (d) Sample characterized by Group B microstructures (PV1448). (c) Overview. (d) A typical Group B microstructure. (e) and (f) Sample characterized by Group C microstructures (PV1437). (e) Overview. (f) A typical Group C microstructure. Note the lack of deformation features in the corona assemblage, especially the pargasite grains.

typically occur in elongate clusters with other pyroxene grains defining the foliation. Both enstatite and diopside grains have exsolutions of rutile needles; enstatite grains commonly have exsolutions of diopside grains (100–900 μm). While many of the pyroxenes retain their rectangular, igneous shapes, evidence for crystal plasticity is common within the grains, which have undulose extinction, deformation twins, and rare subgrains (Figure 2c, red arrows). Ilmenite (ilm, 100-580 μm) is commonly associated with the pyroxene clusters.

Plagioclase grains show some evidence of dynamic recrystallization, where porphyroclasts exhibit undulose extinction and deformation twins (Figure 2c, white arrows) while being surrounded by smaller grains. Brown-green pargasite grains (prg_1) occur either as single coarse grains (up to 1 mm, Figure 2b), or as smaller grains (50–600 μm) in strain shadows around pyroxene grains forming elongate clusters which

define the gneissic foliation with their long axes (Figure 2b, cf. Figure 4b). Pargasite grains also show evidence of crystal plasticity, primarily in the form of undulose extinction (Figure 2c, yellow arrows). The proportion of pargasite is variable at the centimeter to decimeter scale. Pargasite composition is similar for both occurrences with an Mg# of 50–54 and Ti content above 0.20 c.p.f.u. (Figure 3c).

4.2.2. Gabbroic Gneiss With Reaction Microstructures

The reaction microstructures are characterized by grain clusters where remnants of deformed enstatite and diopside grains are surrounded by internally undeformed blue-green pargasite (prg_2) and quartz along pyroxene-plagioclase boundaries (Figure 2b). In direct contact with the pyroxene, prg_2 and quartz are fine grained and symplectitic. In reaction rims of more than 200 μm width, prg_2 occurs as larger grains at the interface to the surrounding plagioclase. Sodic diopside, plagioclase, and clinozoisite are also associated with the reaction microstructures. These compositionally zoned clusters represent coronas, associated with the replacement of the central pyroxene grains. Product phases of the replacement reaction (i.e., prg_2 and quartz) show no significant internal deformation. Furthermore, coronas themselves do not show a shape preferred orientation, especially at a high degree of reaction (Figure 4).

Within samples, the degree of replacement is highly variable (Figure 4). In the following, we describe the replacement microstructures in terms of the proportion of pyroxene replaced by prg_2 + quartz. For ease of description, we distinguish three groups defined by the range of replacement percentage. Group A represents $<$10% replacement (Figures 4a and 4b), Group B 10–80% replacement (Figures 4c and 4d), and Group C $>$ 80% replacement (Figures 4e and 4f). Microstructural and chemical changes from Group A to Group C represent progressive change with increasing degree of replacement.

The chemical composition of replacement related plagioclase (pl_2) and diopside (di_2) exhibits a systematic increase in Na content with increasing degree of replacement (Figures 3a and 3b), while chemical analyses of coronate pargasite grains (prg_2) replacing both enstatite and diopside (di_1) show a small range in Mg# (Mg# = 52–57) and Ti $<$ 0.20 c.p.f.u. The Mg# of replacement pargasites are lower than relict igneous enstatite and diopside (Figure 3c), and fall in the narrow range irrespective of the type of pyroxene they replace. Reactant minerals (pl_1, di_1, en) have mostly depleted REE signatures ($\sim$ 0.1–1 times chondrite; Figure 3d), where plagioclase is the only mineral enriched in LREE (10 times chondrite). In contrast, new pargasite produced in the reaction (prg_2) has flat, enriched REE patterns (10 times chondrite), which are uniform throughout the sample regardless of whether the reactant pyroxene is enstatite or diopside.

4.2.2.1. Group A (<10% Replacement)

Group A microstructures (Figure 4a) are defined by an assemblage of diopside-enstatite-pargasite-plagioclase-clinozoisite-ilmenite in which less than 10% of the original pyroxenes have been replaced. In Group A microstructures, small (50–100 μm) blue-green pargasite (prg_2) grows along enstatite-plagioclase and diopside-plagioclase grain boundaries (Figure 4b). Very rarely, $\sim$50 μm wide, discontinuous bands of symplectitic intergrowths of blue-green pargasite and quartz develop along grain boundaries between pyroxenes and blue-green pargasite. Cuspate volumes of plagioclase and quartz occur at the outer boundary of coronas (Figure 5a). Within the cuspate volumes, thin ($\sim$1–2 μm) films of plagioclase and rarely, K-feldspar, wet pargasite-quartz grain boundaries (Figure 5a). Films may extend up to $\sim$20 μm along grain boundaries, terminating in small dihedral angles. Three-mineral, granitic (K-feldspar, plagioclase, and quartz) aggregates (Figure 5b) also may occur at the outer boundary of coronas. In the aggregates, all three minerals are in contact. Rarely, K-feldspar forms thin films along quartz-plagioclase grain boundaries (Figure 5b).

Surrounding the clusters of pyroxene and pargasite, plagioclase is present with physical and chemical characteristics similar to that of the gabbroic gneiss without replacement microstructures (Figure 3a). Replacement microstructures commonly develop asymmetrically around pyroxene grains (Figure 4a, red arrows). Although they are always found along pyroxene-plagioclase grain boundaries, blue-green pargasite and pargasite-quartz symplectites are discontinuous along the boundaries and may develop only on one side of a pyroxene grain. Similarly, development of these microstructures is not evenly distributed across a thin section, with local variation in grain size and width of coronas and symplectites.

4.2.2.2. Group B (10–80% Replacement)

Different to Group A replacement microstructures, Group B (Figure 4c) shows a significant amount of quartz in its assemblage. In Group B microstructures, between 10–80% of the original pyroxenes have been replaced. Consequently the remnants of igneous pyroxenes (enstatite and diopside, di_1) are smaller than those in Group A (500–1700 μm), with rare coarse grains (up to 3500 μm), and rounded shapes with

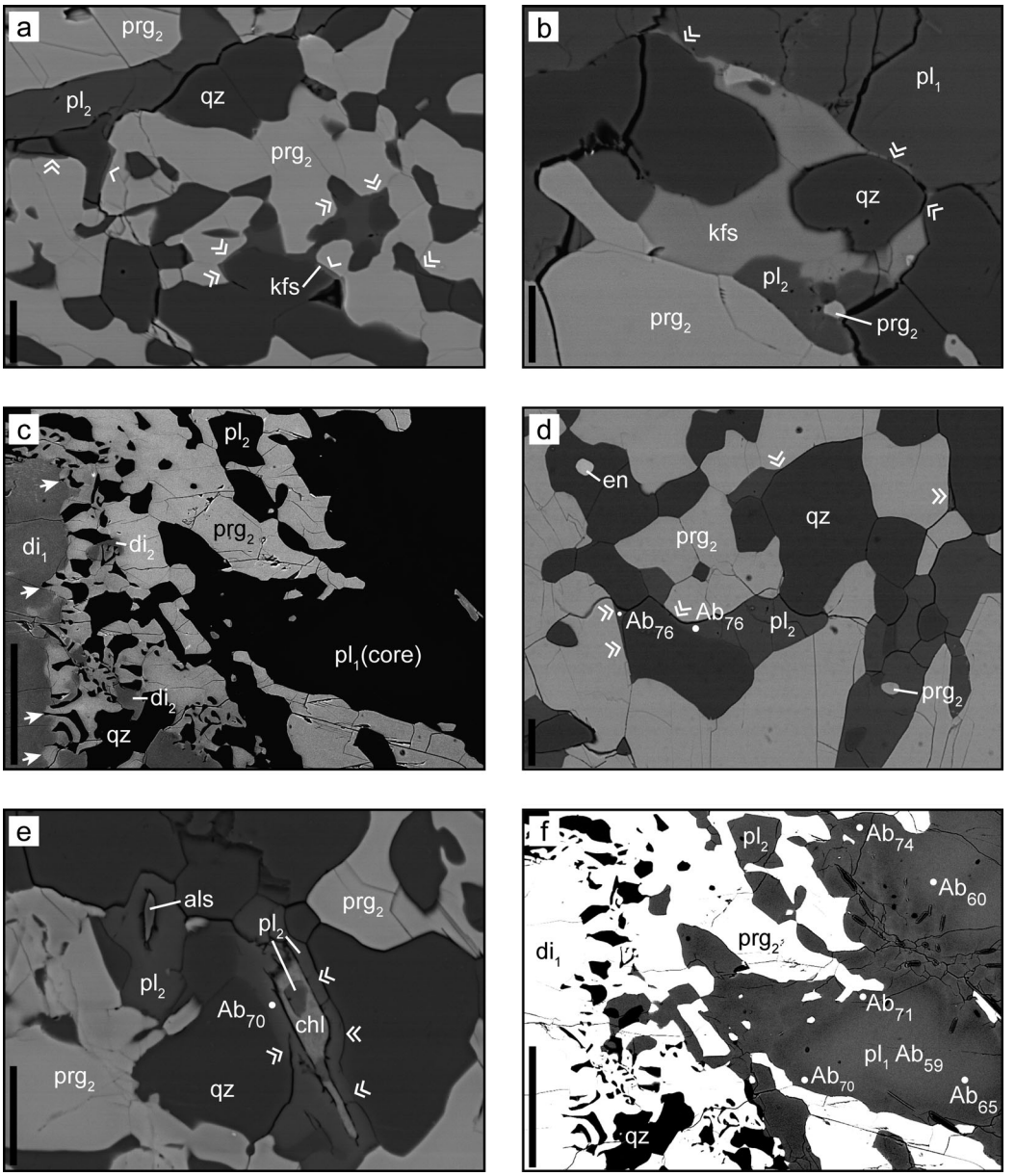

Figure 5. Backscatter electron images of microstructures indicative of the former presence of melt within replacement microstructures. (a) and (b) A Group A microstructure in a sample characterized by Group A microstructures (PV1426). (a) Cuspate volumes of plagioclase and quartz, where plagioclase (double arrows) and K-feldspar (single arrows) wet quartz-pargasite grain boundaries, terminating in low dihedral angles. Scale bar is 20 μm. (b) Three mineral (K-feldspar, plagioclase, and quartz) granitic aggregates at the outer boundary of a corona. Note the K-feldspar wetting plagioclase-quartz grain boundaries. Scale bar is 20 μm. (c)–(e) Group B replacement microstructures in a sample characterized mainly by Group C replacement microstructures (PV1437). (c) Cross section through a corona, from corroded diopside (di_1) on the left to host plagioclase (pl_1) on the right. Note cuspate boundaries of corroded diopside (di_1) filled with pargasite and quartz (white arrows) and secondary diopside (di_2) forming in the corona. Scale bar is 100 μm. (d) Plagioclase forming films, wet grain boundaries and filling triple junctions (pl_2) in the symplectite. Note high albite content (Ab = 100 * [Na/{Ca + Na + K}]) of plagioclase films, and low dihedral angles of plagioclase at pargasite and quartz junctions (double arrows). Scale bar is 20 μm. (e) A film of plagioclase (pl_2) pseudomorphing chlorite (double arrows; the chlorite most likely pseudomorphed biotite, but no relict biotite grain remains). Note the even width of plagioclase film and parallelism of grain boundaries along the right side of the chlorite grain. Scale bar is 20 μm. (f) Zonation of coarse grained plagioclase. Note low Z values of rims of coarse plagioclase grains (pl_1), corresponding to increased albite content.

corroded and cuspate grain boundaries (Figure 5c). The total width of the coronas is between 200 and 700 μm, and symplectitic intergrowths of blue-green pargasite and quartz range in width from 50 to 200 μm. The symplectite may also include a sodic diopside (di_2), particularly adjacent to the corroded pyroxene grain at the center of the corona (Figure 5c). Cuspate volumes of plagioclase and quartz occur at the outer boundary of coronas (Figure 5d). Plagioclase (Ab = 66–73) may form thin (~1–5 μm) films wetting quartz

and pargasite grain boundaries in the outermost part of symplectites (Figure 5d). Films commonly begin at small plagioclase grains filling triple junctions and extend 10–20 μm along grain boundaries, terminating in small dihedral angles. Where they do have films of plagioclase, quartz grains are typically rounded. Plagioclase partially pseudomorphs phyllosilicates, forming thin films (2–5 μm) along grain boundaries (Figure 5e). In this case, grain boundaries of plagioclase are parallel to those of phyllosilicates and plagioclase films are a uniform thickness along each side of the grain. Different to Group A, coarse-grained blue-green pargasite (110–450 μm) always forms the outermost layer of the corona, where it is in contact with the host plagioclase grains.

Different to the unreacted host and Group A, plagioclase grains exhibit a higher fraction of small grains with a distinct more sodic composition (Ab = 65–75; Figure 5f). Small grains show little to no evidence of internal deformation, commonly have multiple twinning and typically have straight grain boundaries with some 120° triple junctions. In places, fine-grained plagioclase have one or two inclusions of clinozoisite needles; however, it is more common for clinozoisite to lie along grain boundaries between grains.

All pyroxenes in Group B microstructures show some development of coronas; however, the extent of development is heterogeneous. It is common for individual pyroxene grains to have wider coronate textures on one side of the grain compared to the other (Figure 4c, red arrows). The degree of corona development can also differ dramatically between adjacent pyroxene grains; while the majority of coronas in Group B microstructures are as described above, there may also be some Group A coronas.

4.2.2.3. Group C (>80% Replacement)

The assemblage of Group C replacement microstructures (Figure 4e) is distinct as pyroxenes are absent, and apatite and rutile are present. Group C microstructures are similar in character to those in Group B; the main difference being that at the center of the corona lies either a small rutile grain, or rarely a remnant pyroxene (100–400 μm) with heavily corroded grain boundaries (Figure 4f). Apatite grains (~100 μm) are typically round and form either within the symplectitic or within the coarser, undeformed blue-green pargasite of the outer corona (Figure 4f). While the blue-green pargasite (prg_2) exhibits the same compositions, the compositional range of plagioclase in the corona is more sodic (Ab = 66–80) compared to the other Groups (Figure 3a). Group C replacement structures also exhibit the cuspate volumes of plagioclase and quartz, with plagioclase wetting quartz-pargasite grain boundaries.

The majority of matrix plagioclase grains (Ab = 57–79) are finer grained than in the other Groups (50–350 μm). Similar to Group B needles of clinozoisite along plagioclase-plagioclase grain boundaries are ubiquitous.

Similar to Groups A and B, the extent of Group C corona development is heterogeneous at both the scale of a thin section and individual corona structures (Figure 4e, red arrows). Different to Group A and B, the shape of replacement microstructures is highly irregular and shows no shape preferred orientation.

5. Patterns of Trace Element Variation Revealed by X-Ray Fluorescence Mapping

The pattern of trace element variations in two samples that are dominated by either Group A or Group C replacement microstructures are shown in Figure 6. Both samples have high Sr concentrations in plagioclase grains, where Group A microstructures range between 1466 and 2933 ppm (Figure 6c), and Group C microstructures between 2035 and 3855 ppm (Figure 6d). Strontium shows a strong local enrichment, both at the scale of the map and at the grain scale.

At the map scale, bands of high Sr plagioclase traverse the thin section, following pyroxene-plagioclase boundaries and are spatially associated with corona development (Figured 6c and 6d). The majority of high Sr bands are parallel to the foliation (Figures 6e and 6f, red arrows). Individual clusters of pyroxenes are connected by high Sr plagioclase "bridges" (Figures 6e and 6f, blue arrows). Concentrations of high Sr plagioclase are also found in embayments in the pyroxene clusters (Figures 6e and 6f, green arrows). These features are easily discerned in Group A microstructures (Figured 6c and 6e), where pyroxene and plagioclase grains are large and Sr enrichment is not localized. In Group C microstructures (Figures 6d and 6f) which have experienced more extensive replacement, individual high Sr bands are not as easily discerned as Sr concentration is elevated throughout the mapped area; however, plagioclase grains around Group C coronas have markedly higher Sr concentrations compared to those around Groups A and B coronas.

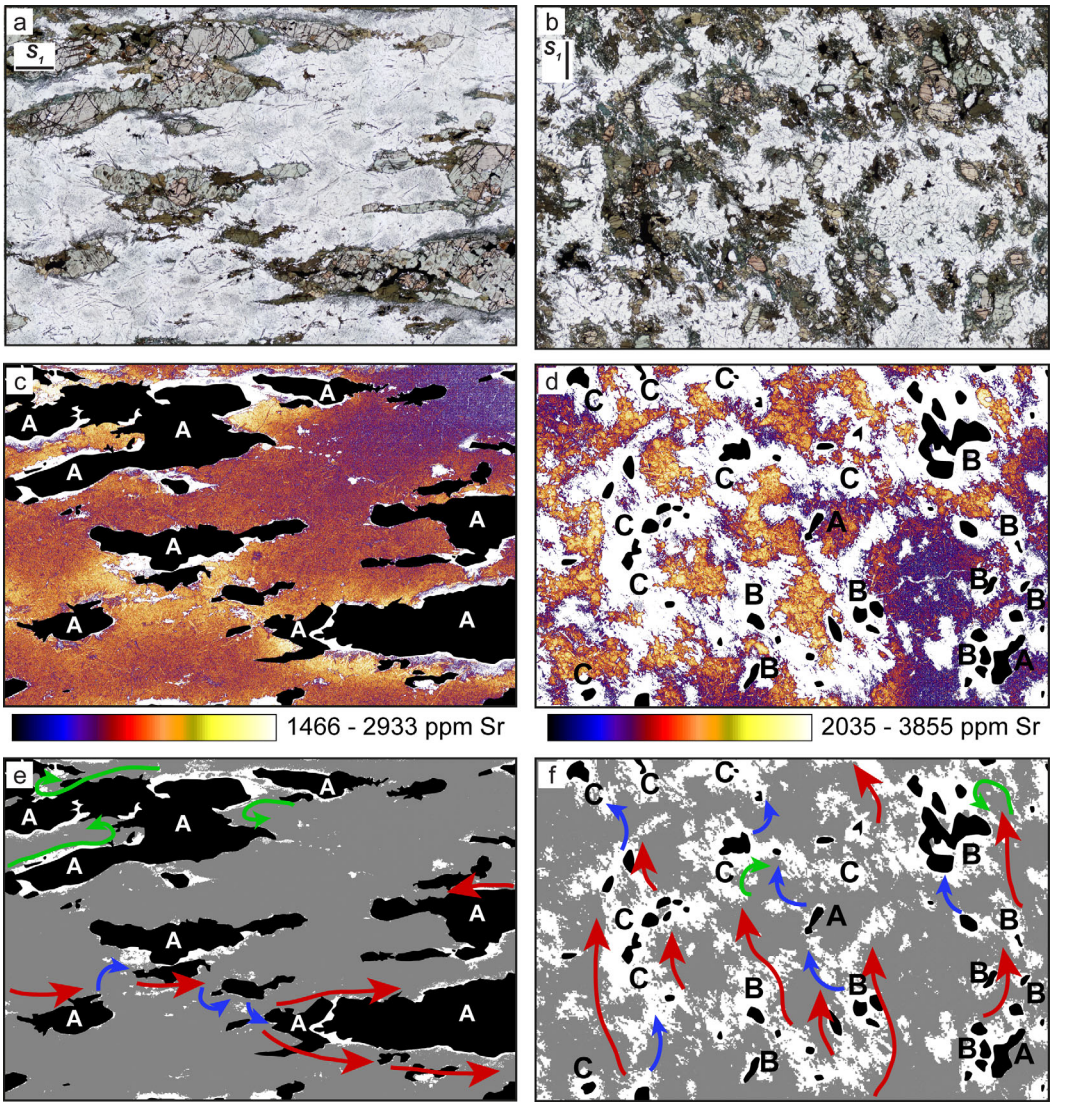

Figure 6. Patterns of Strontium variation. (a) Overview photomicrograph in plain polarized light of a sample characterized by Group A microstructures (PV1426). S_1 orientation marked in top left of images. FOV = 18 mm. (b) Overview photomicrograph in plain polarized light of a sample characterized by Group C microstructures (PV1437). FOV = 12 mm. (c) and (d) Plagioclase Sr concentration of areas shown in Figures 6a and 6b, respectively, with pyroxenes marked in black, replacement microstructures marked in white, and individual microstructures classified into groups. Sr is enriched next to replacement microstructures and in bands connecting individual coronas across samples. (e) and (f) Schematic representation of high Sr bands along plagioclase (grey)-pyroxene/corona boundaries parallel to foliation (red), in embayments (green), and along plagioclase-plagioclase boundaries forming "bridges" (blue) interpreted from Figures 6c and 6d, respectively. Note that bands connect individual coronas across samples.

Zonation of Sr is also observed within individual plagioclase grains, and is commonly asymmetric where plagioclase grains are adjacent to coronas. In Group A microstructures, individual grains are large (0.9–2.0 mm) and show asymmetric Sr zonation forming the high Sr bands (Figure 6c). In Group C microstructures, grain-scale zonation of Sr is stronger, especially adjacent to amphiboles (white), where plagioclase grains commonly have high Sr boundaries next to pargasite, and low Sr boundaries next to other plagioclase grains (Figure 6d).

6. Whole Rock Chemistry

To investigate if there is a systematic change in whole rock chemistry with increasing degree of replacement microstructures, seven samples representing variations in replacement occurrence were analyzed. There are no consistent changes between samples dominated by Group A, B, or C

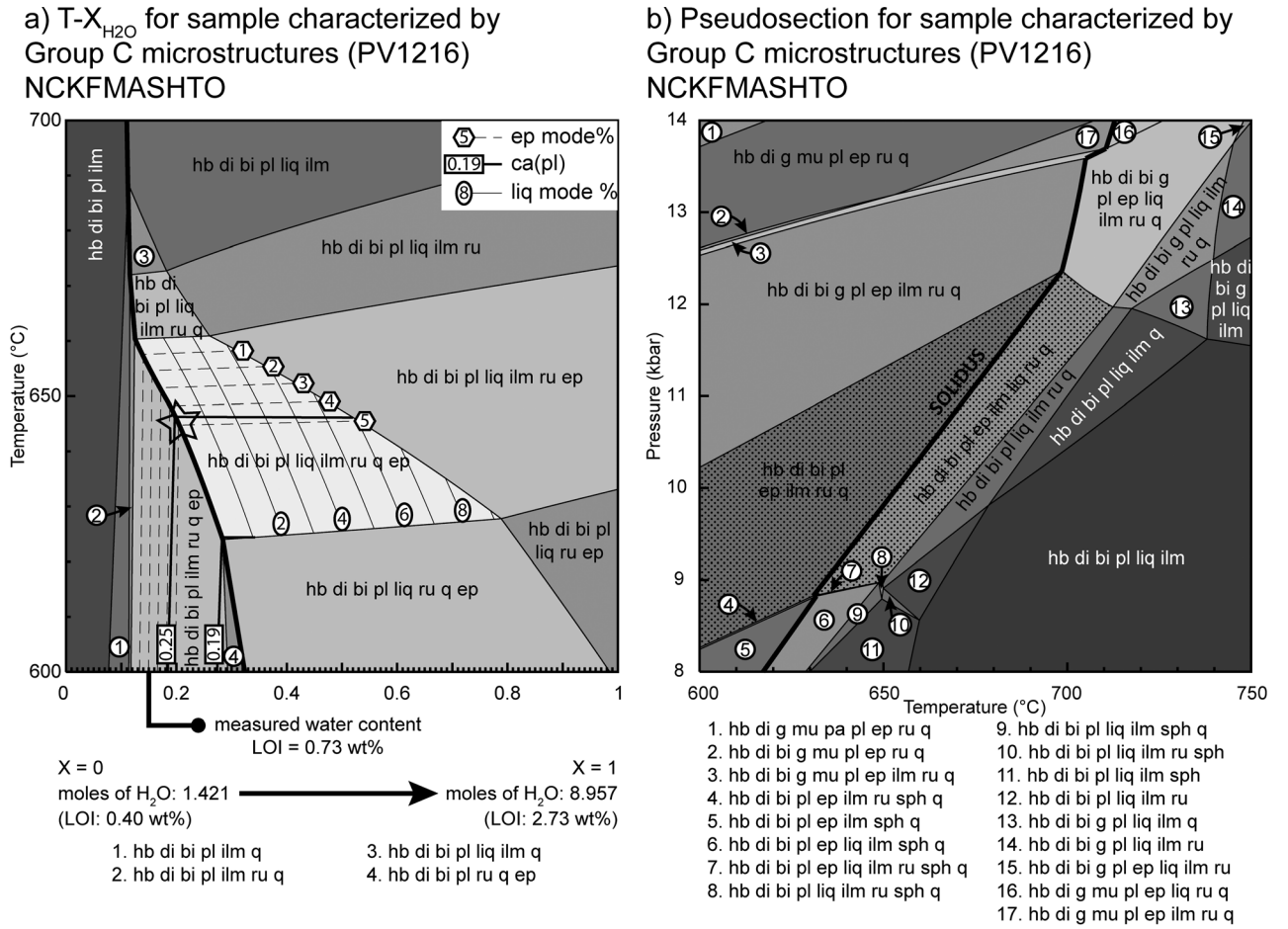

Figure 7. Thermodynamic pseudosection models constructed for a sample characterized by Group C microstructures (PV1216, Table 1). (a) T-X_{H2O} diagram used to constrain water content in the sample at corona-forming conditions. Contoured fields are those where the Group C assemblage (hb + di + bi + pl + ep + ilm + ru + q) is stable. Solidus highlighted in bold. Star indicates the best estimate of conditions, on the solidus where variations in plagioclase composition and epidote proportions in the natural sample overlap in the model. (b) P-T pseudosection; stippled fields are those where the Group C assemblage (hb + di + bi + pl + ep + ilm + ru + q) is stable. Solidus highlighted in bold. (c) Epidote mode proportion, and plagioclase and amphibole compositional contours are plotted for the assemblage hb + di + bi + pl + ep + ilm + ru + q in fields straddling the solidus. The whole field below the solidus has isopleths the same as the one immediately above the solidus, with little change in composition or mode of minerals across that field.

microstructures. However, there is a general correlation between an increase in loss on ignition values, used as a measure of volatile content, and the dominant replacement microstructural Group within the sample. A lack of carbonate minerals in the natural samples, and only small quantities of

F and Cl measured in mineral chemistry analyses, suggests that volatiles other than water are not present in appreciable quantities.

7. P-T Constraints

The constructed P-T pseudosection calculated for a representative sample dominantly exhibiting Group C microstructures is shown in Figure 7b. Regions in P-T space suitable for replacement microstructure formation have the mineral assemblage hb + di + bi + pl + ep + ilm + ru + q, where hb is equivalent to prg_2, di is equivalent to di_2 and pl is equivalent to pl_2. This assemblage is stable both above and below the solidus, between temperatures of <600 and 710°C, and pressures of 8.2 and 12.4 kbar. These two fields are constrained on three sides by the lack of epidote at higher temperatures, the addition of titanite (sph) at lower pressures and the addition of garnet at higher pressures (Figure 7b).

Plots of epidote mode proportion, amphibole compositional contours x(hb) [$Fe^{2+}/(Fe^{2+} + Mg)$] and plagioclase compositional contours ca(pl) [Ca/(Ca + Na + K)] for both subsolidus and supersolidus fields are presented in Figure 7c. Below the solidus, mineral chemistry and epidote mode proportion are relatively stable over the range of temperatures and pressures, with the mode of ep < 6%, and the compositional variables x(hb) < 0.385 and ca(pl) > 0.24. Above the solidus, the mineral chemistry and mode proportion of epidote are more variable in the model; contour lines are parallel to the solidus and changes occur over small temperature and pressure intervals. Measured values from the sample indicate the replacement microstructures formed at conditions with ep ≤ 6%, x(hb) = 0.34–0.37 and ca(pl) = 0.19–0.25, ranging above and below the solidus. Consequently, the observed assemblage is stable in the upper amphibolite facies, close to the solidus.

8. Discussion

8.1. Conditions for Replacement Microstructure Development

Detailed microstructural analysis shows that the formation of the replacement microstructures (i.e., coronas) did not occur while the rocks were deforming in either the brittle or ductile regime, as newly grown prg_2 and quartz show neither significant internal deformation nor dynamic recrystallization. In addition, asymmetric replacement microstructures do not preferentially grow in strain shadows, nor do they show any shape preferred orientation. In contrast, unreacted minerals in the gabbroic gneiss show distinct solid state deformation features. These include the presence of elongate clusters of pyroxene and pargasite (prg_1) which show crystal bending and deformation twinning characteristic of solid state deformation (Figure 2c) [*Passchier and Trouw*, 2005]. The same solid state deformation is observed in unreacted plagioclase grains with large, internally deformed porphyroclasts surrounded by small, recrystallized grains. Consequently, corona formation postdates the development of the gneissic foliation and occurred under static conditions.

The replacement assemblage records local hydration, with hydrous mineral proportions increasing from Group A to Group C. In association with replacement microstructures, plagioclase grains are enriched in Sr and Na, and on a broader scale, plagioclase chemistry changes toward a more albitic composition (Figure 3a). Pargasite (prg_2) associated with the replacement microstructures in samples taken throughout the whole outcrop shows a remarkably homogeneous Mg# and REE enrichment, regardless of whether they replace enstatite or diopside (Figure 3c).

Systematic changes in chemistry with increasing degree of replacement regardless of the phase being replaced as well as the remarkably homogeneous prg_2 Mg# and REE chemistry points to an open chemical system during replacement, where pargasite chemistry is effectively buffered but plagioclase and diopside chemistry is not. Consistent chemical trends throughout samples from the whole outcrop suggest that the chemical system was open to fluid migration at least at the kilometer scale, focusing attention on whether the hydrous fluid is an aqueous fluid or silicate melt. Pseudosection analysis shows that the assemblage hb + di + bi + pl + ep + ilm + ru + q which characterizes the replacement microstructures is stable near the solidus within a wide temperature and pressure range of < 600–710°C and 8.2–12.4 kbar. Microstructures indicative of the former presence of melt and geochemical observations discussed below resolve this ambiguity.

8.2. Process of Corona Formation

Classic corona formation involves subsolidus lattice diffusion of elements between two reactant minerals, triggered by changes in P-T conditions. As a result, product minerals form at the interface between the reactant minerals. Since lattice diffusion rates within a grain are near-homogeneous, replacement products form a continuous and symmetric corona at the interface [e.g., *Gallien et al*., 2012; *Grant*, 1988; *Markl et al*., 1998; *Mongkoltip and Ashworth*, 1983]. For these coronas, a closed chemical system is assumed, allowing determination of diffusion coefficients of different elements [e.g., *Markl et al*., 1998], and P-T paths of corona formation [e.g., *Griffin*, 1971]. Based on the fact that corona development in the Pembroke Granulite (i) is typically asymmetric, and in the extreme case discontinuous along a single pyroxene-plagioclase boundary (Group A microstructures), (ii) involves hydration, and (iii) occurs in a chemically open system, corona formation must have occurred by a different process.

Coronate features similar to those described here have been observed in other plutonic bodies, where anhydrous minerals are partially replaced by a hydrous assemblage [e.g., *Acquafredda et al*., 1992, *Beard et al*., 2004; *Zibra*, 2006]. Such features are interpreted to form during the final stages of crystallization via a reaction between anhydrous minerals crystallized early in the pluton (e.g. pyroxene, Fe-Ti oxides) and the remnant melt, in which water is concentrated. Early studies on the Pembroke Granulite briefly describe the amphibole coronas and attribute their formation to a late stage magmatic alteration [*Blattner*, 1976]. However, here we demonstrate that replacement microstructures and associated Sr enrichment postdate the subsolidus formation of the gneissic foliation. Therefore, the observed hydration is unlikely to be a result of hydration of the pluton during late-stage crystallization.

Many conventional interpretations of retrograde hydration involving corona-type structures advocate the infiltration of an aqueous fluid, resulting in a hydration reaction [e.g., *Ashworth et al*., 1992; *Broadhurst*, 1986; *Joesten*, 1986; *Liu et al*., 2013]. Here, we use an intimate spatial relationship between hydrous reaction products and microstructures indicative of the former presence of melt, along with the enriched REE chemistry of product pargasite (prg_2) throughout the gabbroic gneiss to discount the involvement of an aqueous fluid. Additionally, at calculated conditions above solidus for the Pembroke Granulite, the introduction of $\sim$1.5 wt.% of an aqueous fluid would result in the production of large volumes of melt ($\geq$10%) through the volume-negative consumption of plagioclase, epidote, and quartz [e.g., *Clemens and Droop*, 1998; *Gardien et al*., 2000; *Sawyer*, 2010]. Samples examined lack field, microstructural, or chemical evidence for voluminous partial melting, and so the presence of an aqueous fluid is deemed unlikely within the calculated P-T window.

Figure 5 shows five microstructural criteria indicative of the former presence of melt [*Holness and Sawyer*, 2008; *Vernon*, 2011]: (i) three-mineral, granitic (K-feldspar, plagioclase, and quartz) aggregates where all three minerals are in contact (Figures 5a and 5b); (ii) dihedral angles of $\leq$60° where a grain of plagioclase meets grains of quartz and pargasite, or where a grain of quartz meets two pargasite grains (where the portion of the grain forming the small dihedral angle is inferred to have pseudomorphed former melt; Figures 5a and 5d); (iii) cuspate volumes of quartz and sodic plagioclase (Figures 5a, 5d, and 5f); (iv) phyllosilicate minerals pseudomorphed by plagioclase (Figure 5e); (v) films of plagioclase that are more sodic than plagioclase elsewhere in the rock (Figures 5d and 5e). These observations demonstrate the reactant fluid was silicate melt, and preclude aqueous fluid infiltration. The occurrence of microstructures indicative of the former presence of melt in all samples (Groups A–C) shows that even limited hydration (Group A) occurred supersolidus and involved the infiltration of silicate melt.

In support of the microstructural criteria, enriched mineral REE data for product pargasite (prg_2) in comparison to reactant pyroxenes (en and di_1) and plagioclase (pl_1; Figure 3d) indicates an open system involving the infiltration of silicate melt. These enriched patterns are uniform throughout the sample and can only be explained by reaction of the depleted plagioclase and enstatite grains with a REE-enriched fluid. Experiments show that REE do not partition favorably into aqueous fluid but partition much more favorably into silicate melt [*Adam et al*., 2014; *Cullers et al*., 1973; *Flynn and Burnham*, 1978; *Wendlandt and Harrison*, 1979]. Though the type of fluid in the pseudosection modeling is ambiguous, these microstructural and mineral geochemical observations indicate supersolidus P-T conditions for corona formation (630–710°C, 8.8–12.4 kbar; Figure 7b).

Even though mineral chemistry within replacement microstructures indicates an open chemical system, the lack of trends in whole rock chemical data indicates limited metasomatism at the hand sample scale. While

the exact chemistry of the reaction cannot be calculated, several defining characteristics can be deduced: (1) replacement microstructures are limited to pyroxene-plagioclase boundaries (Figures 4a, 4c, and 4e); (2) hydration requires a source of H_2O; (3) product pargasite grains have homogeneous Mg#, lower than the parent pyroxene, and uniformly enriched REE content (Figures 3c and 3d); (4) product plagioclase grains are enriched in albite content (Figure 3a); (5) product plagioclase grains are enriched in Sr (Figures 6c and 6d). Together with the microstructures, mineral geochemistry and calculated P-T conditions (Figure 7b), the above observations suggest the replacement reaction involves pyroxene, plagioclase, and a silicate melt as reactants. The following reaction accounts for the observed chemical and mineralogical changes

$$\begin{aligned} &\mathrm{di}_1(\mathrm{Mg\#} = 0.72\text{–}0.89) + \mathrm{en}\ (\mathrm{Mg\#} = 0.57\text{–}0.64) + \mathrm{pl}_1(\mathrm{Sr} \\ &\quad \leq 2000\ \mathrm{ppm},\ \mathrm{Ab} = 54\text{–}62) + \mathrm{melt}_1 = \mathrm{prg}_2(\mathrm{Mg\#} = 0.47\text{–}0.57) + \mathrm{qtz} + \mathrm{pl}_2(\mathrm{Sr} \\ &\quad \geq 2000\ \mathrm{ppm},\ \mathrm{Ab} = 66\text{–}80) + \mathrm{melt}_2 \pm \mathrm{di}_2(\mathrm{Mg\#} = 0.68\text{–}0.73) \end{aligned}$$

Accordingly, the melt is inferred to have an intermediate composition, being Sr-H_2O-Na-rich and Mg-poor relative to the gabbroic gneiss. Reaction-scale metasomatism is recognized in the mineral geochemistry patterns. However, the partial reaction of precursor minerals limits recognition of metasomatism at the hand sample scale. Additionally, the natural variation in major and trace element composition of the protolith (Group A samples, Table 1) is of the same magnitude as that expected for reaction-scale metasomatism. Limited metasomatism suggests most melt passed through the gabbroic gneiss, reacting along grain boundary pathways, and little remained to noticeably change the bulk rock composition.

8.3. Origins of the Chemical Signature Associated With Corona Formation: A Regional Perspective

The enriched REE content of product pargasite (prg_2) indicates reaction involving silicate melt. High Sr-Na arc magmas, such as the interpreted reactant melt, are generated through partial melting of the feldspar-absent, garnet-bearing lower crust [*Chapman et al*., 2016; *Stevenson et al*., 2005; *Tulloch and Kimbrough*, 2003], conditions not achieved in the Pembroke Granulite (Figure 7) thus precluding local incipient melting as a melt source. Instead the reactant melt must have been produced in a deeper part of the Fiordland crust and migrated to higher crustal levels. During upward migration, the progressive decrease in pressure and temperature would lower the solubility of H_2O in the melt [*Holtz et al*., 1995], with available H_2O facilitating melt-rock reactions and amphibole production [*Davidson et al*., 2007; *Smith*, 2014]. Large volumes of high Sr-Na magmas were emplaced in the Fiordland lower and middle crust between 126 and 105 Ma [*Chapman et al*., 2016; *Tulloch and Kimbrough*, 2003], including the dioritic to tonalitic Separation Point Suite and the ultramafic to dioritic Western Fiordland Orthogneiss (Figure 1). Compositional variations in these suites are postulated to be due to modification during segregation from their source rock [*Allibone et al*., 2009b; *Getsinger et al*., 2009]. However, our observations point to an alternative model for such intrabatholith chemical variations where fractions of these high Sr-Na melts migrated at km scales through the Pembroke Granulite and equivalent lower crust, with chemical modification occurring during migration contributing to the spread in Sr-Na bulk rock compositions in the younger suites (Figure 1b). This is supported by observations of partial replacement microstructures of pyroxene grains to amphibole and quartz in all low strain Arthur River Complex exposures (e.g. Stirling Falls, Lake Pukutahi, Mt Daniel) [*Daczko et al*., 2002a, 2002b], and reports of coronate microstructures characterized by amphibole around corroded pyroxene elsewhere in Fiordland [*Allibone et al*., 2009a, 2009b], which may also record movement of melt through the crust.

8.4. Reaction Microstructures As Indicators for Melt Transfer in Lower Crustal Rocks

Our observations suggest mass transfer in an open chemical system where transport of silicate melt occurs along grain boundaries, forming microstructures produced by the reaction of a hydrous silicate melt and the largely anhydrous high grade assemblage of the host rock. We propose that mass transfer occurred via diffuse porous flow of a migrating, reactive melt. The correlation of Sr-Na enrichment in plagioclase grains with the development of replacement microstructures suggest that patterns in Sr-Na enrichment trace high Sr-Na melt pathways. These pathways are interconnected and strongly controlled by pyroxene-plagioclase boundary connectivity and distribution, resulting in a flow dominantly along the pre-existing foliation (Figures 6e and 6f). At the petrographic scale, melt pathways can be recognized by observation of reaction microstructures. For example, melt is inferred to have migrated along grain boundaries with reaction microstructures, while grain boundaries devoid of reaction microstructures saw little melt transport. This interpretation is supported by the observation of asymmetric corona development, which indicate one side of a pyroxene grain was adjacent to a melt pathway, while the other was not. The lack of detectable

metasomatic signature and areas of significant changes in assemblage at a centimeter to meter scale supports a diffuse rather than channelized pervasive mass transfer.

Although commonly invoked as a mechanism for local melt segregation and accumulation in the crust, until now evidence for diffuse porous flow on a large scale through crustal rocks has been limited. Diffuse porous flow in the crust is considered to be too slow to be an efficient migration mechanism over large scales [*McKenzie*, 1984]. Because the viscosity contrast between the host rock and migrating melt is not as large as that in the mantle, porous flow in the crust is thought to be largely deformation driven [*Hasalová et al*., 2008c]. In addition, melt migration at the grain scale would only be sustainable if the temperature of the melt and the host are similar, in order to prevent freezing of the melt and arresting of diffuse porous flow. So far, numerical models have focused on exploring the conditions at which it is possible to extract melt from a partially molten rock. For example, numerical models of melt segregation from source rocks in a contact aureole setting [*Fountain et al*., 1989; *Jackson and Cheadle*, 1998; *Jackson et al*., 2005] show that melt can flow up to 2.6 km along grain boundaries, if a porosity is first created by up to 50% partial melting. *Solano et al*. [2012] suggest that diffuse porous flow is only an effective melt extraction mechanism if the melt fraction (i.e., porosity) is in the order of 20%. *Hasalová et al*. [2008a] showed evidence for a geological setting where externally derived melt is injected into a porous rock and stagnates, producing ubiquitous frozen-in melt microstructures. To our knowledge, there is no study that explicitly explores the geological scenario of mass transfer along grain boundaries that is not deformation-driven in the crustal environment. However, in the mantle environment, melt transfer and associated millimeter to meter-scale metasomatism has been widely discussed [*Kelemen et al*., 1997].

In our view, a rock at and just above its solidus with minor proportions of internally derived incipient melt ($<$5%) would create a permeable, interconnected network throughout the solid framework of the rock. As the incipient partial melt migrates upward, an external melt could utilize the existing permeable grain boundary network to infiltrate the rock and transfer to higher crustal levels. High water contents in the externally derived melt would decrease viscosity by several orders of magnitude, promoting movement through the network without necessitating deformation to drive flow. In this scenario, at any one time only small amounts of melt are present in the solid rock. Once established the interconnected network may be reused again and again. Such reuse will result in minimal metasomatic signatures as the melt transfers along the same pathways, where reaction has already taken place. The interconnected, permeable grain boundary network can be maintained even if P-T conditions change, as long as the host rock remains just above the solidus. Mass transfer can therefore be sustained over an extended period of time, allowing significant amounts of melt to move through the solid rock causing large-scale chemical homogenization. The vertical and horizontal scale of mass transfer by an external melt would be limited by the extent of partial melting within the host rock, which is in turn dictated by the vertical temperature gradient. As the source of the external melt is physically depleted and fluid pressure gradients drop, some silicate melt is left in the fluxed host rocks. These crystallize and preserve delicate microstructural evidence for the former presence of melt.

Despite a lack of evidence for widespread partial melting in the Pembroke Granulite, pseudosection modeling supports the production of small ($<$3%) melt fractions at calculated P-T conditions (Figure 7). The formation of grain boundary permeability and melt mobility at very low melt fractions ($<$4% in the mantle, $\sim$7% in the crust) is supported by theoretical and experimental data [e.g., *Faul*, 2001; *Menegon et al*., 2011; *Negrini et al*., 2014; *Rosenberg and Handy*, 2005; *Waff and Bulau*, 1979; *Zhu et al*., 2011], so calculated volumes of partial melting could feasibly create permeability within the Pembroke Granulite if small degrees of partial melting ($<$3%) are weakly focused into channels at all scales. The porosity created by incipient partial melting along with the creation of a variably connected melt network allowed the transfer of the externally derived, hydrous, Sr-Na-rich melt through the Pembroke Granulite. In this scenario, metasomatism would be limited to the grain scale, mass transfer is diffuse but penetrative, and is sustainable within a significant portion of the lower crust, as the assemblage associated with melt-rock reaction is stable over a large P-T window.

Here we propose that the described replacement microstructures with their characteristics of (i) asymmetric development, (ii) chemical homogeneity, (iii) hydrous reaction products intergrown with felsic minerals showing microstructures indicative of the former presence of melt, (iv) a pattern of variable development at the centimeter to meter scale, (v) clear spatial association with trace element patterns, and (vi) a static

nature can be used as indicators for diffuse porous melt flow in the lower crust. Importantly, such diffuse porous melt flow is only sustainable and effective if the host maintains a permeable grain boundary network, provided through incipient, low degree melting. The fact that similar microstructures have been reported throughout the arc environment of Fiordland, New Zealand [*Allibone et al*., 2009b] suggests that this process may have occurred over an area of ~12,000 km^2. Thus, incipient melt assisted diffuse porous melt flow may represent a significant melt transfer process.

9. Conclusions

Partial replacement microstructures in the Pembroke Granulite involve a hydrous silicate melt in an open chemical environment. Interconnected grain boundary networks, created by incipient partial melting, facilitated the kilometer-scale transfer of an externally derived, reactive melt via diffuse porous flow. A process of diffuse porous flow is interpreted from the variable development of asymmetric, undeformed replacement microstructures, which have homogeneous mineral chemistry on a large scale and are spatially associated with trace element patterns. These microstructures and mineral chemistry of the Pembroke Granulite represent an exceptional example of preservation of pathways of efficient mass transfer via diffuse porous flow assisted by incipient partial melting in the lower crust. Diffuse porous flow therefore has the potential to be an important mechanism of mass transfer in the lower crust, affecting host rock microstructure and the chemical evolution of lower crustal magmas.

Acknowledgments
ARC Future Fellowship (FT110100070) to S.P. and Discovery Project funding (DP120102060 and DP170103946) to S.P. and NRD provided financial support to conduct this research. We thank the Department of Conservation, New Zealand for permission to visit and sample localities in the Fiordland National Park. Reviews by L. Menegon and one anonymous reviewer helped to greatly improve the manuscript. Comments by S. Foley, R. Weinberg and others are greatly appreciated. Part of this research was undertaken on the X-Ray Fluorescence Microscopy beamline at the Australian Synchrotron, Victoria, Australia. This work was supported by the Multi-modal Australian ScienceS Imaging and Visualisation Environment (MASSIVE) (www.massive.org.au). This study used instrumentation funded by ARC LIEF and DEST Systemic Infrastructure Grants, Macquarie University and Industry. This is contribution 842 from the ARC Centre of Excellence for Core to Crust Fluid Systems (www.ccfs.mq.edu.au) and 1103 from the GEMOC Key Centre (www.gemoc.mq.edu.au).

References

Acquafredda, P., A. Caggianelli, and G. Piccarreta (1992), Late magmatic to subsolidus coronas in gabbroic rocks from the Sila Massif (Calabria, Italy), *Mineral. Petrol.*, *46*(3), 229–238.

Adam, J., M. Locmelis, J. C. Afonso, T. Rushmer, and M. L. Fiorentini (2014), The capacity of hydrous fluids to transport and fractionate incompatible elements and metals within the Earth's mantle, *Geochem. Geophys. Geosyst.*, *15*, 2241–2253, doi:10.1002/2013GC005199.

Allibone, A. H., L. A. Milan, N. R. Daczko, and I. M. Turnbull (2009a), Granulite facies thermal aureoles and metastable amphibolite facies assemblages adjacent to the Western Fiordland Orthogneiss in southwest Fiordland, New Zealand, *J. Metamorph. Geol.*, *27*(5), 349–369.

Allibone, A. H., R. Jongens, I. M. Turnbull, L. A. Milan, N. R. Daczko, M. C. DePaoli, and A. J. Tulloch (2009b), Plutonic rocks of Western Fiordland, New Zealand: Field relations, geochemistry, correlation, and nomenclature, *N. Z. J. Geol. Geophys.*, *52*(4), 379–415.

Allibone, A. H., R. Jongens, J. M. Scott, A. J. Tulloch, I. M. Turnbull, A. F. Cooper, N. G. Powell, E. B. Ladley, R. P. King, and M. S. Rattenbury (2009c), Plutonic rocks of the Median Batholith in eastern and central Fiordland, New Zealand: Field relations, geochemistry, correlation, and nomenclature, *N. Z. J. Geol. Geophys.*, *52*(2), 101–148.

Ashworth, J. R., J. J. Birdi, and T. F. Emmett (1992), Diffusion in coronas around clinopyroxene: Modelling with local equilibrium and steady state, and a non-steady-state modification to account for zoned actinolite-hornblende, *Contrib. Mineral. Petrol.*, *109*(3), 307–325.

Beach, A., and W. S. Fyfe (1972), Fluid transport and shear zones at Scourie, Sutherland: Evidence of overthrusting?, *Contrib. Mineral. Petrol.*, *36*(3), 175–180.

Beard, J. S., P. C. Ragland, and T. Rushmer (2004), Hydration crystallization reactions between anhydrous minerals and hydrous melt to yield amphibole and biotite in igneous rocks: Description and implications, *J. Geol.*, *112*(5), 617–621.

Beere, W. (1975), A unifying theory of the stability of penetrating liquid phases and sintering pores, *Acta Metall.*, *23*(1), 131–138.

Blattner, P. (1976), Replacement of hornblende by garnet in granulite facies assemblages near Milford Sound, New Zealand, *Contrib. Mineral. Petrol.*, *55*(2), 181–190.

Blattner, P. (1991), The north Fiordland transcurrent convergence, *N. Z. J. Geol. Geophys.*, *34*(4), 533–542.

Bouilhol, P., J. A. D. Connolly, and J.-P. Burg (2011), Geological evidence and modeling of melt migration by porosity waves in the sub-arc mantle of Kohistan (Pakistan), *Geology*, *39*(12), 1091–1094.

Bourdon, E., J.-P. Eissen, M. Monzier, C. Robin, H. Martin, J. Cotten, and M. L. Hall (2002), Adakite-like lavas from Antisana Volcano (Ecuador): Evidence for slab melt metasomatism beneath Andean Northern Volcanic Zone, *J. Petrol.*, *43*(2), 199–217.

Broadhurst, J. R. (1986), Mineral reactions in xenoliths from the Colorado Plateau; implications for lower crustal conditions and fluid composition, *Geol. Soc. Spec. Publ.*, *24*(1), 331–349.

Brown, M. (2004), The mechanism of melt extraction from lower continental crust of orogens, *Geol. Soc. Am. Spec. Pap.*, *389*, 35–48.

Carter, K. E., and S. I. Dworkin (1990), Channelized fluid flow through shear zones during fluid-enhanced dynamic recrystallization, Northern Apennines, Italy, *Geology*, *18*(8), 720–723.

Cartwright, I., and A. C. Barnicoat (2003), Geochemical and stable isotope resetting in shear zones from Täschalp: Constraints on fluid flow during exhumation in the Western Alps, *J. Metamorph. Geol.*, *21*(2), 143–161.

Chadam, J., D. Hoff, E. Merino, P. Ortoleva, and A. Sen (1986), Reactive infiltration instabilities, *IMA J. Appl. Math.*, *36*(3), 207–221.

Chapman, T., G. L. Clarke, N. R. Daczko, S. Piazolo, and A. Rajkumar (2015), Orthopyroxene–omphacite- and garnet–omphacite-bearing magmatic assemblages, Breaksea Orthogneiss, New Zealand: Oxidation state controlled by high-P oxide fractionation, *Lithos*, *216–217*, 1–16.

Chapman, T., G. L. Clarke, and N. R. Daczko (2016), Crustal differentiation in a thickened arc: Evaluating depth dependences, *J. Petrol.*, *57*(3), 595–620.

Clarke, G. L., K. A. Klepeis, and N. R. Daczko (2000), Cretaceous high-*P* granulites at Milford Sound, New Zealand: Metamorphic history and emplacement in a convergent margin setting, *J. Metamorph. Geol.*, *18*(4), 359–374.

Clarke, G. L., N. R. Daczko, K. A. Klepeis, and T. Rushmer (2005), Roles for fluid and/or melt advection in forming high-*P* mafic migmatites, Fiordland, New Zealand, *J. Metamorph. Geol.*, *23*(7), 557–567.

Clarke, G. L., N. Daczko, and D. Miescher (2013), Identifying Relic Igneous Garnet and Clinopyroxene in Eclogite and Granulite, Breaksea Orthogneiss, New Zealand, *J. Petrol.*, *54*(9), 1921–1938.
Clemens, J. D., and G. T. R. Droop (1998), Fluids, *P–T* paths and the fates of anatectic melts in the Earth's crust, *Lithos*, *44*(1), 21–36.
Coggon, R., and T. J. B. Holland (2002), Mixing properties of phengitic micas and revised garnet-phengite thermobarometers, *J. Metamorph. Geol.*, *20*(7), 683–696.
Connolly, J. A. D., and Y. Y. Podladchikov (2007), Decompaction weakening and channeling instability in ductile porous media: Implications for asthenospheric melt segregation, *J. Geophys. Res.*, *112*, B10205, doi:10.1029/2005JB004213.
Cullers, R. L., L. G. Medaris, and L. A. Haskin (1973), Experimental studies of the distribution of rare earths as trace elements among silicate minerals and liquids and water, *Geochim. Cosmochim. Acta*, *37*(6), 1499–1512.
Daczko, N. R., and J. A. Halpin (2009), Evidence for melt migration enhancing recrystallization of metastable assemblages in mafic lower crust, Fiordland, New Zealand, *J. Metamorph. Geol.*, *27*(2), 167–185.
Daczko, N. R., K. A. Klepeis, and G. L. Clarke (2001a), Evidence of Early Cretaceous collisional-style orogenesis in northern Fiordland, New Zealand and its effects on the evolution of the lower crust, *J. Struct. Geol.*, *23*(4), 693–713.
Daczko, N. R., G. L. Clarke, and K. A. Klepeis (2001b), Transformation of two-pyroxene hornblende granulite to garnet granulite involving simultaneous melting and fracturing of the lower crust, Fiordland, New Zealand, *J. Metamorph. Geol.*, *19*(5), 549–562.
Daczko, N. R., G. L. Clarke, and K. A. Klepeis (2002a), Kyanite-paragonite-bearing assemblages, northern Fiordland, New Zealand: Rapid cooling of the lower crustal root to a Cretaceous magmatic arc, *J. Metamorph. Geol.*, *20*(9), 887–902.
Daczko, N. R., J. A. Stevenson, G. L. Clarke, and K. A. Klepeis (2002b), Successive hydration and dehydration of high-*P* mafic granofels involving clinopyroxene-kyanite symplectites, Mt Daniel, Fiordland, New Zealand, *J. Metamorph. Geol.*, *20*, 669–682.
Davidson, J., S. Turner, H. Handley, C. Macpherson, and A. Dosseto (2007), Amphibole "sponge" in arc crust?, *Geology*, *35*(9), 787–790.
De Paoli, M. C., G. L. Clarke, and N. R. Daczko (2012), Mineral Equilibria Modeling of the Granulite–Eclogite Transition: Effects of Whole-Rock Composition on Metamorphic Facies Type-Assemblages, *J. Petrol.*, *53*(5), 949–970.
Diener, J. F. A., R. Powell, R. W. White, and T. J. B. Holland (2007), A new thermodynamic model for clino-and orthoamphiboles in the system Na_2O–CaO–FeO–MgO–Al_2O_3–SiO_2–H_2O–O, *J. Metamorph. Geol.*, *25*(6), 631–656.
Dijkstra, A. H., M. G. Barth, M. R. Drury, P. R. D. Mason, and R. L. M. Vissers (2003), Diffuse porous melt flow and melt-rock reaction in the mantle lithosphere at a slow-spreading ridge: A structural petrology and LA-ICP-MS study of the Othris Peridotite Massif (Greece), *Geochem. Geophys. Geosyst.*, *4*(8), 8613, doi:10.1029/2001GC000278.
Esawi, E. K. (2004), AMPH-CLASS: An Excel spreadsheet for the classification and nomenclature of amphiboles based on the 1997 recommendations of the International Mineralogical Association, *Comput. Geosci.*, *30*(7), 753–760.
Faul, U. H. (2001), Melt retention and segregation beneath mid-ocean ridges, *Nature*, *410*(6831), 920–923.
Flynn, R. T., and W. C. Burnham (1978), An experimental determination of rare earth partition coefficients between a chloride containing vapor phase and silicate melts, *Geochim. Cosmochim. Acta*, *42*(6), 685–701.
Fountain, J. C., D. S. Hodge, and R. P. Shaw (1989), Melt segregation in anatectic granites: A thermo-mechanical model, *J. Volcanol. Geotherm. Res.*, *39*(4), 279–296.
Fujii, N., K. Osamura, and E. Takahashi (1986), Effect of water saturation on the distribution of partial melt in the Olivine-Pyroxene-Plagioclase System, *J. Geophys. Res.*, *91*(B9), 9253–9259.
Gallien, F., A. Mogessie, C. A. Hauzenberger, E. Bjerg, S. Delpino, and B. Castro De Machuca (2012), On the origin of multi-layer coronas between olivine and plagioclase at the gabbro–granulite transition, Valle Fértil–La Huerta Ranges, San Juan Province, Argentina, *J. Metamorph. Geol.*, *30*(3), 281–302.
Gardien, V., A. B. Thompson, and P. Ulmer (2000), Melting of Biotite + Plagioclase + Quartz Gneisses: The Role of H_2O in the Stability of Amphibole, *J. Petrol.*, *41*(5), 651–666.
Gardner, R. L., S. Piazolo, and N. R. Daczko (2016), Shape of pinch and swell structures as a viscosity indicator: Application to lower crustal polyphase rocks, *J. Struct. Geol.*, *88*, 32–45.
Getsinger, A., T. Rushmer, M. D. Jackson, and D. Baker (2009), Generating High Mg-numbers and Chemical Diversity in Tonalite–Trondhjemite–Granodiorite (TTG) Magmas during Melting and Melt Segregation in the Continental Crust, *J. Petrol.*, *50*(10), 1935–1954.
Godard, M., J.-L. Bodinier, and G. Vasseur (1995), Effects of mineralogical reactions on trace element redistributions in mantle rocks during percolation processes: A chromatographic approach, *Earth Planet. Sci. Lett.*, *133*(3), 449–461.
Grant, S. M. (1988), Diffusion models for corona formation in metagabbros from the Western Grenville Province, Canada, *Contrib. Mineral. Petrol.*, *98*(1), 49–63.
Gray, C. M., and A. I. S. Kemp (2009), The two-component model for the genesis of granitic rocks in southeastern Australia: Nature of the metasedimentary-derived and basaltic end members, *Lithos*, *111*(3–4), 113–124.
Green, E., T. Holland, and R. Powell (2007), An order-disorder model for omphacitic pyroxenes in the system jadeite-diopside-hedenbergite-acmite, with applications to eclogitic rocks, *Am. Mineral.*, *92*(7), 1181–1189.
Griffin, W. L. (1971), Genesis of coronas in anorthosites of the upper jotun Nappe, Indre Sogn, Norway, *J. Petrol.*, *12*(2), 219–243.
Griffin, W. L., W. J. Powell, N. J. Pearson, and S. Y. O'Reilly (2008), GLITTER: Data reduction software for laser ablation ICP-MS, in edited by P. Sylvester, Laser Ablation-ICP-MS in the Earth Sciences: Mineralogical Association of Canada Short Course Series, vol. 40, Appendix 2, pp. 204–207.
Hasalová, P., V. Janoušek, K. Schulmann, P. Štípská, and V. Erban (2008a), From orthogneiss to migmatite: Geochemical assessment of the melt infiltration model in the Gföhl Unit (Moldanubian Zone, Bohemian Massif), *Lithos*, *102*(3), 508–537.
Hasalová, P., P. Štípská, R. Powell, K. Schulmann, V. Janoušek, and O. Lexa (2008b), Transforming mylonitic metagranite by open-system interactions during melt flow, *J. Metamorph. Geol.*, *26*(1), 55–80.
Hasalová, P., K. Schulmann, O. Lexa, P. Štípská, F. Hrouda, S. Ulrich, J. Haloda, and P. Týcová (2008c), Origin of migmatites by deformation-enhanced melt infiltration of orthogneiss: A new model based on quantitative microstructural analysis, *J. Metamorph. Geol.*, *26*(1), 29–53.
Holland, T. J. B., and R. Powell (1998), An internally consistent thermodynamic data set for phases of petrological interest, *J. Metamorph. Geol.*, *16*(3), 309–343.
Holland, T. J. B., and R. Powell (2011), An improved and extended internally consistent thermodynamic dataset for phases of petrological interest, involving a new equation of state for solids, *J. Metamorph. Geol.*, *29*(3), 333–383.
Hollis, J. A., G. L. Clarke, K. A. Klepeis, N. R. Daczko, and T. R. Ireland (2003), Geochronology and geochemistry of high-pressure granulites of the Arthur River Complex, Fiordland, New Zealand: Cretaceous magmatism and metamorphism on the palaeo-Pacific Margin, *J. Metamorph. Geol.*, *21*(3), 299–313.

Holness, M. B., and E. W. Sawyer (2008), On the pseudomorphing of melt-filled pores during the crystallization of migmatites, *J. Petrol.*, *49*(7), 1343–1363.
Holtz, F., H. Behrens, D. B. Dingwell, and W. Johannes (1995), H_2O solubility in haplogranitic melts: Compositional, pressure, and temperature dependence, *Am. Mineral.*, *80*, 94–108.
Holyoke, C. W. I., and T. Rushmer (2002), An experimental study of grain scale melt segregation mechanisms in two common crustal rock types, *J. Metamorph. Geol.*, *20*(5), 493–512.
Jackson, M. D., and M. J. Cheadle (1998), A continuum model for the transport of heat, mass and momentum in a deformable, multicomponent mush, undergoing solid-liquid phase change, *Int. J. Heat Mass Transfer*, *41*(8), 1035–1048.
Jackson, M. D., M. J. Cheadle, and M. P. Atherton (2003), Quantitative modeling of granitic melt generation and segregation in the continental crust, *J. Geophys. Res.*, *108*(B7), 2332, doi:10.1029/2001JB001050.
Jackson, M. D., K. Gallagher, N. Petford, and M. J. Cheadle (2005), Towards a coupled physical and chemical model for tonalite–trondhjemite–granodiorite magma formation, *Lithos*, *79*(1–2), 43–60.
Joesten, R. (1986), The role of magmatic reaction, diffusion and annealing in the evolution of coronitic microstructure in troctolitic gabbro from Risör, Norway, *Mineral. Mag.*, *50*(357), 441–467.
Keay, S., W. J. Collins, and M. T. McCulloch (1997), A three-component Sr-Nd isotopic mixing model for granitoid genesis, Lachlan fold belt, eastern Australia, *Geology*, *25*(4), 307–310.
Kelemen, P. B., G. Hirth, N. Shimizu, M. Spiegelman, and H. J. Dick (1997), A review of melt migration processes in the adiabatically upwelling mantle beneath oceanic spreading ridges, *Philos. Trans. R. Soc. London A*, *355*(1723), 283–318.
Kelley, K. A., and E. Cottrell (2009), Water and the oxidation state of subduction zone magmas, *Science*, *325*(5940), 605–607.
Korhonen, F., M. Brown, C. Clark, J. D. Foden, and R. Taylor (2015), Are granites and granulites consanguineous?, *Geology*, *43*(11), 991–994.
Leake, B. E., et al. (1997), Nomenclature of amphiboles: Report of the Subcommittee on Amphiboles of the International Mineralogical Association, Commission on New Minerals and Mineral Names, *Eur. J. Mineral.*, *35*, 219–246.
Liu, Q., J. Hermann, and J. Zhang (2013), Polyphase inclusions in the Shuanghe UHP eclogites formed by subsolidus transformation and incipient melting during exhumation of deeply subducted crust, *Lithos*, *177*, 91–109.
Markl, G., C. T. Foster, and K. Bucher (1998), Diffusion-controlled olivine corona textures in granitic rocks from Lofoten, Norway: Calculation of Onsager diffusion coefficients, thermodynamic modelling and petrological implications, *J. Metamorph. Geol.*, *16*(5), 607–623.
McKenzie, D. (1984), The generation and compaction of partially molten rock, *J. Petrol.*, *25*(3), 713–765.
Menegon, L., P. Nasipuri, H. Stünitz, H. Behrens, and E. Ravna (2011), Dry and strong quartz during deformation of the lower crust in the presence of melt, *J. Geophys. Res.*, *116*, B10410, doi:10.1029/2011JB008371.
Mongkoltip, P., and J. R. Ashworth (1983), Quantitative estimation of an open-system symplectite-forming reaction: Restricted diffusion of al and si in coronas around olivine, *J. Petrol.*, *24*(4), 635–661.
Moresi, L., and H. B. Mühlhaus (2006), Anisotropic viscous models of large-deformation Mohr–Coulomb failure, *Philos. Mag.*, *86*(21-22), 3287–3305.
Morimoto, N. (1988), Nomenclature of Pyroxenes, *Mineral. Petrol.*, *39*(1), 55–76.
Mortimer, N., A. J. Tulloch, R. N. Spark, N. W. Walker, E. Ladley, A. Allibone, and D. L. Kimbrough (1999), Overview of the Median Batholith, New Zealand: A new interpretation of the geology of the Median Tectonic Zone and adjacent rocks, *J. Afri. Earth Sci.*, *29*(1), 257–268.
Negrini, M., H. Stünitz, P. Nasipuri, L. Menegon, and L. F. Morales (2014), Semibrittle deformation and partial melting of perthitic K-feldspar: An experimental study, *J. Geophys. Res. Solid Earth*, *119*, 3478–3502, doi:10.1002/2013JB010573.
Passchier, C. W., and R. A. J. Trouw (2005), *Microtectonics*, Springer, Berlin.
Paterson, D., et al. (2011), The X-ray fluorescence microscopy beamline at the Australian synchrotron, *AIP Conf. Proc.*, *1365*(1), 219–222.
Petford, N. (1996), Dykes or diapirs?, *Earth Environ. Sci. Trans. R. Soc. Edinburgh*, *87*(1-2), 105–114.
Phipps Morgan, J., and B. K. Holtzman (2005), Vug waves: A mechanism for coupled rock deformation and fluid migration, *Geochem. Geophys. Geosyst.*, *6*, Q08002, doi:10.1029/2004GC000818.
Powell, R., and T. J. B. Holland (1988), An internally consistent dataset with uncertainties and correlations: 3. Applications to geobarometry, worked examples and a computer program, *J. Metamorph. Geol.*, *6*(2), 173–204.
Rapp, R. P., N. Shimizu, and M. D. Norman (2003), Growth of early continental crust by partial melting of eclogite, *Nature*, *425*(6958), 605–609.
Rasband, W. S. (1997−2015), ImageJ, U. S. Natl. Inst. of Health, Bethesda, Md. [Available at http://imagej.nih.gov/ij/.]
Richet, P., A.-M. Lejeune, F. Holtz, and J. Roux (1996), Water and the viscosity of andesite melts, *Chem. Geol.*, *128*(1), 185–197.
Rosenberg, C. L., and M. R. Handy (2005), Experimental deformation of partially melted granite revisited: Implications for the continental crust, *J. Metamorph. Geol.*, *23*(1), 19–28.
Ryan, C. G. (2000), Quantitative trace element imaging using PIXE and the nuclear microprobe, *Int. J. Imaging Syst. Technol.*, *11*(4), 219–230.
Ryan, C. G., D. R. Cousens, S. H. Sie, W. L. Griffin, G. F. Suter, and E. Clayton (1990), Quantitative pixe microanalysis of geological matemal using the CSIRO proton microprobe, *Nucl. Instrum. Methods Phys. Res. Sect. B*, *47*(1), 55–71.
Ryan, C. G., D. N. Jamieson, C. L. Churms, and J. V. Pilcher (1995), A new method for on-line true-elemental imaging using PIXE and the proton microprobe, *Nucl. Instrum. Methods Phys. Res. Sect. B*, *104*(1), 157–165.
Ryan, C. G., B. E. Etschmann, S. Vogt, J. Maser, C. L. Harland, E. Van Achterbergh, and D. Legnini (2005), Nuclear microprobe–synchrotron synergy: Towards integrated quantitative real-time elemental imaging using PIXE and SXRF, *Nucl.Instrum. Methods in Phys. Res. Sect. B*, *231*(1), 183–188.
Ryan, C. G., et al. (2010a), The new Maia detector system: Methods for high definition trace element imaging of natural material, paper presented at X-RAY OPTICS AND MICROANALYSIS: Proceedings of the 20th International Congress, AIP Conference Series, Karlsruhe, Germany.
Ryan, C. G., R. Kirkham, R. M. Hough, G. Moorhead, D. P. Siddons, M. D. De Jonge, D. J. Paterson, G. De Geronimo, D. L. Howard, and J. S. Cleverley (2010b), Elemental X-ray imaging using the Maia detector array: The benefits and challenges of large solid-angle, *Nucl. Instrum. Methods Phys. Res. Sect. A*, *619*(1), 37–43.
Sawyer, E. W. (2010), Migmatites formed by water-fluxed partial melting of a leucogranodiorite protolith: Microstructures in the residual rocks and source of the fluid, *Lithos*, *116*(3–4), 273–286.
Schröter, F. C., J. A. Stevenson, N. R. Daczko, G. L. Clarke, N. J. Pearson, and K. A. Klepeis (2004), Trace element partitioning during high-P partial melting and melt-rock interaction; An example from northern Fiordland, New Zealand, *J. Metamorph. Geol.*, *22*(5), 443–457.
Schulze, F., H. Behrens, F. Holtz, J. Roux, and W. Johannes (1996), The influence of H_2O on the viscosity of a haplogranitic melt, *Am. Mineral.*, *81*, 1155–1165.

Scott, D. R., and D. J. Stevenson (1986), Magma ascent by porous flow, *J. Geophys. Res.*, *91*(B9), 9283–9296.
Scott, D. R., D. J. Stevenson, and J. A. Whitehead Jr. (1986), Observations of solitary waves in a viscously deformable pipe, *Nature*, *319*(6056), 759–761.
Shaw, H. R. (1972), Viscosities of magmatic silicate liquids; an empirical method of prediction, *Am. J. Sci.*, *272*(9), 870–893.
Sleep, N. H. (1988), Tapping of melt by veins and dikes, *J. Geophys. Res.*, *93*(B9), 10,255–10,272.
Smith, D. J. (2014), Clinopyroxene precursors to amphibole sponge in arc crust, *Nat. Commun.*, *5*, 4329.
Smith, J. R., S. Piazolo, N. R. Daczko, and L. Evans (2015), The effect of pre-tectonic reaction and annealing extent on behaviour during subsequent deformation: Insights from paired shear zones in the lower crust of Fiordland, New Zealand, *J. Metamorph. Geol.*, *33*(6), 557–577.
Solano, J. M. S., M. D. Jackson, R. S. J. Sparks, J. D. Blundy, and C. Annen (2012), Melt segregation in deep crustal hot zones: A mechanism for chemical differentiation, crustal assimilation and the formation of evolved magmas, *J. Petrol.*, *53*(10), 1999–2026.
Soustelle, V., A. Tommasi, J. L. Bodinier, C. J. Garrido, and A. Vauchez (2009), Deformation and Reactive melt transport in the mantle lithosphere above a large-scale partial melting domain: The Ronda Peridotite Massif, Southern Spain, *J. Petrol.*, *50*(7), 1235–1266.
Spence, D. A., P. W. Sharp, and D. L. Turcotte (1987), Buoyancy-driven crack propagation: A mechanism for magma migration, *J. Fluid Mech.*, *174*(1), 135–153.
Spiegelman, M., and P. Kenyon (1992), The requirements for chemical disequilibrium during magma migration, *Earth Planet. Sci. Lett.*, *109*(3–4), 611–620.
Stevenson, J. A., N. R. Daczko, G. L. Clarke, N. Pearson, and K. A. Klepeis (2005), Direct observation of adakite melts generated in the lower continental crust, Fiordland, New Zealand, *Terra Nova*, *17*(1), 73–79.
Stowell, H., A. Tulloch, C. Zuluaga, and A. Koenig (2010), Timing and duration of garnet granulite metamorphism in magmatic arc crust, Fiordland, New Zealand, *Chem. Geol.*, *273*(1-2), 91–110.
Streit, J. E., and S. F. Cox (1998), Fluid infiltration and volume change during mid-crustal mylonitization of Proterozoic granite, King Island, Tasmania, *J. Metamorph. Geol.*, *16*(2), 197–212.
Sturm, R. (2002), PX-NOM - an interactive spreadsheet program for the computation of pyroxene analyses derived from the electron microprobe, *Comput. Geosci.*, *28*(4), 473–483.
Taylor, S. R., and S. M. McLennan (1995), The geochemical evolution of the continental crust, *Rev. Geophys.*, *33*(2), 241–265.
Tetley, M. G., and N. R. Daczko (2014), Virtual Petrographic Microscope: A multi-platform education and research software tool to analyse rock thin-sections, *Aust. J. Earth Sci.*, *61*(4), 631–637.
Tulloch, A. J., and D. L. Kimbrough (2003), Paired plutonic belts in convergent margins and the development of high Sr/Y magmatism: Peninsular Ranges Batholith of Baja California and Median Batholith of New Zealand, *Geol. Soc. Am. Spec. Pap.*, *374*, 275–295.
Tulloch, A. J., T. Ireland, D. Kimbrough, W. Griffin, and J. Ramezani (2011), Autochthonous inheritance of zircon through Cretaceous partial melting of Carboniferous plutons: The Arthur River Complex, Fiordland, New Zealand, *Contrib. Mineral. Petrol.*, *161*(3), 401–421.
Turcotte, D. L., and J. L. Ahern (1978), A porous flow model for magma migration in the asthenosphere, *J. Geophys. Res.*, *83*(B2), 767–772.
Vanderhaeghe, O. (1999), Pervasive melt migration from migmatites to leucogranite in the Shuswap metamorphic core complex, Canada: Control of regional deformation, *Tectonophysics*, *312*(1), 35–55.
Vanderhaeghe, O. (2009), Migmatites, granites and orogeny: Flow modes of partially-molten rocks and magmas associated with melt/solid segregation in orogenic belts, *Tectonophysics*, *477*(3–4), 119–134.
Vernon, R. H. (2011), Microstructures of melt-bearing regional metamorphic rocks, *Geol. Soc. Am. Mem.*, *207*, 1–11.
Vigneresse, J. L. (2006), Granitic batholiths: From pervasive and continuous melting in the lower crust to discontinuous and spaced plutonism in the upper crust, *Earth Environ. Sci. Trans. R. Soc. Edinburgh*, *97*(04), 311–324.
von Bargen, N., and H. S. Waff (1986), Permeabilities, interfacial areas and curvatures of partially molten systems: Results of numerical computations of equilibrium microstructures, *J. Geophys. Res.*, *91*(B9), 9261–9276.
Waff, H. S., and J. R. Bulau (1979), Equilibrium fluid distribution in an ultramafic partial melt under hydrostatic stress conditions, *J. Geophys. Res.*, *84*(B11), 6109–6114.
Weinberg, R. F. (1996), Ascent mechanism of felsic magmas: News and views, *Earth Environ. Sci. Trans. R. Soc. Edinburgh*, *87*(1-2), 95–103.
Weinberg, R. F., and M. P. Searle (1998), The Pangong Injection Complex, Indian Karakoram: A case of pervasive granite flowthrough hot viscous crust, *J. Geol. Soc.*, *155*(5), 883–891.
Wendlandt, R. F., and W. J. Harrison (1979), Rare earth partitioning between immiscible carbonate and silicate liquids and CO_2 vapor: Results and implications for the formation of light rare earth-enriched rocks, *Contrib. Mineral. Petrol.*, *69*(4), 409–419.
White, R. W., R. Powell, T. J. B. Holland, and B. A. Worley (2000), The effect of TiO_2 and Fe_2O_3 on metapelitic assemblages at greenschist and amphibolite facies conditions: Mineral equilibria calculations in the system K_2O-FeO-MgO-Al_2O_3-SiO_2-H_2O-TiO_2-Fe_2O_3, *J. Metamorph. Geol.*, *18*(5), 497–512.
White, R. W., R. Powell, and G. Clarke (2002), The interpretation of reaction textures in Fe-rich metapelitic granulites of the Musgrave Block, central Australia: Constraints from mineral equilibria calculations in the system K_2O–FeO–MgO–Al_2O_3–SiO_2–H_2O–TiO_2–Fe_2O_3, *J. Metamorph. Geol.*, *20*(1), 41–55.
White, R. W., R. Powell, and T. J. B. Holland (2007), Progress relating to calculation of partial melting equilibria for metapelites, *J. Metamorph. Geol.*, *25*(5), 511–527.
Zhu, W., G. A. Gaetani, F. Fusseis, L. G. J. Montési, and F. De Carlo (2011), Microtomography of partially molten rocks: Three-dimensional melt distribution in mantle peridotite, *Science*, *332*(6025), 88–91.
Zibra, I. (2006), Late-Hercynian granitoid plutons emplaced along a deep crustal shear zone. A case study from the S. Lucia nappe (Alpine Corsica, France), Univ. di Pisa, Pisa, Italy.